## Utrecht University

Master Thesis Earth, Surface & Water

# Pore Network Model Extraction and the Impact of Fractures on Permeability and Solute Transport

Author                       **Martijn van Leer**

Student number        **4120973**

Supervisor               **Dr. Amir Raoof**

Second supervisor     **Prof. Dr. Ruud Schotting**

Utrecht, 28-06-2019

# Table of Contents

## Abstract

In this thesis, first, a new method for pore network extraction is proposed, which is later used to model heterogeneous fractures through a sample, to obtain the effects of fractures on permeability and solute transport properties of porous media. The pore network extraction method combines features from the medial axis method, the maximal ball method, and the axis ball method. We found that, the method provides good results for permeability for sandstones and carbonates, given sufficiently good imaging resolution and a large enough sample sizes are used. In the extracted model a fracture is constructed using a regular grid with different apertures. Heterogeneity is created by disconnecting pores within the fracture plane. Permeability is increased quadratically with increasing aperture size. Improved connectivity caused by the fracture increases the permeability with more than the estimated permeability of the fractured rock, estimated with the weighted arithmetic mean of the permeability of the sample and the permeability of the fracture. Solute transport through the fracture results in increasingly skewed breakthrough curves with long tailing. The dispersivity is increased for medium sized apertures, while high apertures decrease the dispersivity values, as the intrinsic dispersivity of the fracture becomes a preferential flow path. Clogging the fracture results in less variability in dispersivity, as the intrinsic dispersivity of the fracture is larger. The balance between heterogeneity of the fracture and the level of preferential flow through the fracture determine the dispersivity of a fractured medium. Permeabilities in heterogeneous fractures, with varying apertures and clogging, can be approximated with a homogeneous fracture, with a single aperture and no clogging, by using a smaller aperture. Dispersivity changes differ for different clogging fractions of the fracture and cannot be approximated by a homogeneous fracture.

# 1. Introduction

The effect of human activities in the subsurface environments is becoming increasingly important. The subsurface is mainly used to extract or to store energy, with applications such as extraction of fossil fuels, geothermal energy, aquifer thermal energy storage (ATES) and carbon capture storage. In order to improve production, fluid injection methods are used to fracture the subsurface. These processes influence the flow and transport properties of the porous medium. It is important to quantify the effect of such fractures in order to improve the predictivity of the applied models. Previous research focuses mainly on fractures caused by geological processes or human interference at the field and meso scales, while pore scale processes were often not considered. Pore scale research on fractures has been conducted, but have not touched on the subject of the process of fracturing, but mainly on preexisting fractures (e.g., Hughes & Blunt, 2001, Tartakovsky et al., 2007, Jiang et al., 2017). Pore scale research focused on generating fractures is limited and has not focused on clogging or solute transport effects, even though it is important for different applications.

The objective of this study is to obtain the flow and transport properties of rocks prior to as well as after fracturing, with different fracture apertures and different clogging fractions. First, from 3D tomography images a pore network is extracted, by developing a pore network extraction model based on the existing methods. Next this model will be validated using experimental data, to ensure the model works sufficiently. This network will be input for PoreFlow (Raoof et al., 2013) to simulate flow through the network, to obtain the permeabilities as well as solute breakthrough curves. The same is done for the same samples with fractures with different clogging fractions. The results will provide quantitative results for the effect of fracturing and clogging in terms of permeabilities, breakthrough curves and dispersivities.

The following research questions will be answered in this study:

1. How does the permeability change caused by fractures with different apertures compare to the original sample permeability?
2. What is the effect of fractures on solute transport through the sample?
3. How does clogging affect the flow and transport behavior in a fractured sample?
4. Can a heterogeneous fracture be approximated with a homogeneous fracture but with a different aperture?

# 2. Literature Review

## 2.1. Pore Network Modelling

Pore scale modeling is a good method to study pore scale processes and how they manifest themselves in the macroscopic level (Raoof et al., 2013), without assuming homogeneity or being highly dependent on initial and boundary conditions. The pore space with its complex geometry and topology are handled realistically in the way they occur in the rock. Particle methods like the lattice Boltzmann method (Hao & Cheng, 2010, Zhang et al., 2014) use the exact geometry and topology of the pores, but are therefore computationally heavy, and can only be used for small scales and a limited amount of pore volumes (Xiong et al., 2016). Pore network models simplify the geometry of junctions into pore bodies, and the connection in between as pore throats (Jiang et al., 2007), while maintaining the topology as much as possible, which reduces computational time, so it can be used on larger scales with more pores and a higher level of heterogeneity. These models are widely used for single- and multiphase flow and reactive transport. How well the models perform is dependent on the method used to generate the pore network, and how representative this is for the actual rock.

### 2.1.1. Pore Network Properties

How well a pore network model performs is dependent on the topology and geometry, and how well these match the topology and geometry of the porous medium it represents (Vogel and Roth, 2001). Topology covers the location of the pore space, and how they are connected (Joekar-Niasar and Hassanizadeh, 2012). Geometry defines the shape and size of the pores (Xiong et al, 2016).

#### 2.1.1.1. Topology

The topology of a pore network mainly influences the permeability and capillary entry pressure, which are the main fluid flow characteristics of a porous medium. Important parameters that represent the topology are the coordination number distribution and the Euler characteristics (Xiong et al. 2016). The coordination number of a pore is the amount of other pores it is connected to. A higher average coordination number means pores are better connected. The coordination number distribution can vary widely between porous media, depending on porosity, grain size distribution and rock type. Previous research has shown that the mean coordination number of sandstones is 4 (Thovert et al., 1993; Lindquist et al., 1996; Bakke and Oren, 1997; Oren et al., 1997; Oren and Bakke, 2002), but can range up to a maximum of 16. Coordination number distributions do not show the fact that a rock sample can have different disconnected branches, loops and caves, which will decrease the connectivity. The Euler characteristic (Hadwiger, 1957) is a parameter that takes these into account, but does not give any indication on local connectivity. The Euler characteristic is given by the following equation:

$$X_V = \frac{N - C + H}{V} \quad (1)$$

In which $X_v$ is the Euler characteristic number [$L^{-3}$], N is the amount of isolated branches, C is the amount of loops [-] and H is the amount of completely enclosed cavities [-], and V is the volume [$L^3$]. $X_v$ decreases with increasing connectivity. This function gives a single value for the overall topology of the structure, which is equal for a pore network and for the actual pore space, which makes it an important parameter to accurately extract a pore network from 3D images. The combination of the Euler characteristic and the coordination number give a well-defined indication of the topology of a medium.

The topology of a 3D porous medium can be represented in a pore network in both a structured and an unstructured grid. A structured grid has pore bodies at equal distance from each other, divided equally over the space of the model. In an unstructured grid the pores can be located at any given location within the boundaries of the model. Structured grids are used for stochastically reconstructed

models of which no direct topological data is available, as it is easier to match the stochastic data that is available. Euler characteristic numbers and coordination number distributions can directly be represented in a structured grid. Unstructured grids are mainly used when direct topological data is at hand, which can directly be represented in the model (Xiong et al., 2016).

The networks can also be represented with a regular or irregular lattice. A regular lattice has an equal coordination number for every pore, while an irregular lattice has varying coordination numbers.
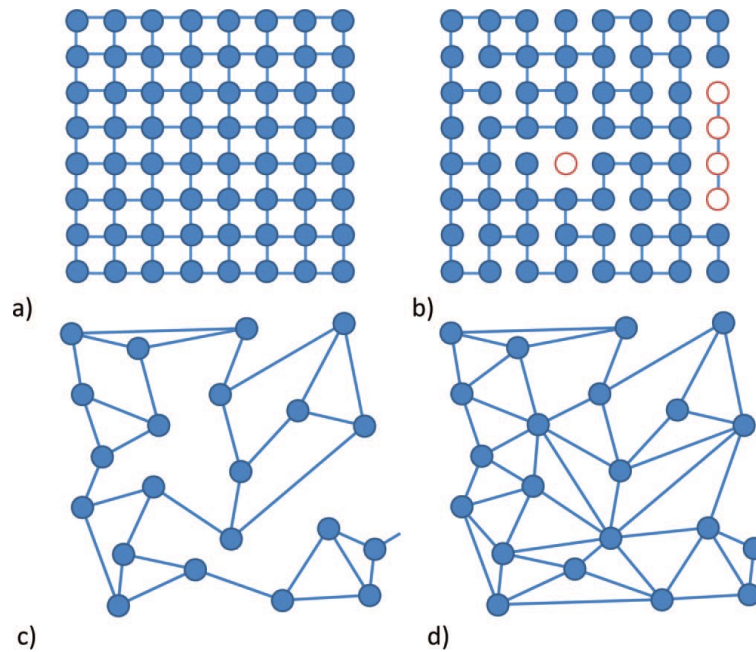


*Figure 1. 2D visualization of possible topologies of pore networks. a) regular structured b) irregular structured c) regular unstructured d) irregular unstructred (Raoof and Hassanizadeh, 2009)*

### 2.1.1.2. Geometry

The geometry of the pore space is defined as the shape and size of pore bodies and throats. The size is important for single phase flow simulations and solute transport, as the residence time in a certain pore body is limited by the cross section of the pore throats (Raoof and Hassanizadeh, 2012) and its tortuosity. Most of the water at a given moment is retained in a pore body, which means solute transport is highly dependent on the amount of mass of solute a pore body is able to hold at a given time. In multiphase flow the shape of the pore throats play an important role, as the wettability of the phases causes the wetting phase to flow through the corners and crevices of the throats, while the non-wetting phase flows through the centre of the throat (Lenormand et al., 1983). This process causes the cross section of the pore throat to not only influence the flow rate, but also the connectivity of the different phases (Raoof and Hassanizadeh, 2012). The shape of a pore throat can be described by the following, considering a 2D cross-section (Mason & Morrow, 1991):

$$G = \frac{A}{P^2} \qquad (2)$$

In which G is the dimensionless shape factor, A is the area $[L^2]$, and P is the perimeter [L]. The maximum value of the shape is 0.08, which correlates with a circle, which is the shape with the highest area compared to its perimeter. As a real throat has a complex geometry, the shape factor can also be described in a 3D tube (Dong & Blunt, 2009):

$$G = \frac{VL}{A^2} \qquad (3)$$

In which V is the volume of the tube [L³], L is the length of the tube [L], and A is the area of the tube [L²]. The values from equation (2) and equation (3) are the same for a given shape, when assumed the 2D shape is the same for the cross section of the total pore throat. Bultreys et al. (2018) use a scale independent method, that does not change depending on resolution:

$$G = \frac{R^2}{4A} \qquad (4)$$

In which $R$ is the inscribed sphere radius [L] and A is the cross sectional area of the throat [L]. This method solves problems caused by square pixels or cubic voxels, which can not have rounded corners or diagonal lines. The values from equation (2), equation (3) and equation (4) are the same for a given shape, when assumed the 2D shape is the same for the cross section of the total pore throat.
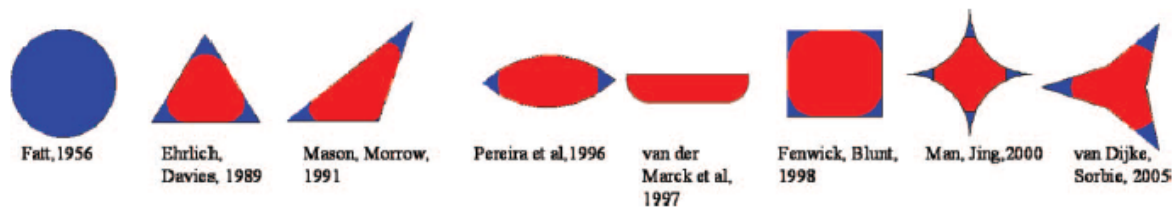


Fatt, 1956 — Ehrlich, Davies, 1989 — Mason, Morrow, 1991 — Pereira et al, 1996 — van der Marck et al, 1997 — Fenwick, Blunt, 1998 — Man, Jing, 2000 — van Dijke, Sorbie, 2005

*Figure 2. Shapes considered in various studies, with wetting phases(blue) and non-wetting phases (red) (Joekar-Niasar & Hassanizadeh, 2012).*

Any shape factor value can have multiple matching shapes, which has to be considered in multiphase flow simulations. Generally the C-T-S approach is used, which uses circles, squares, and triangles with differing angles (Oren et al., 1998, Patzek, 2001, Blunt, 2001).. Joekar-Niasar et al. (2010) has shown the amount of vertices also impacts the permeability of the wetting phase through a pore, meaning the shape factor cannot directly be related to the hydraulic properties of the throat. This can be achieved by taken into account the inscribed sphere of the cross-section, which gives an indication of the concavity of the pore, which can be related to the specific polygon (Hou et al., 2018) or to star shapes with varying amounts of corners (Hellend et al., 2008).

### 2.1.2. Pore network construction

The performance of a pore network depends on the level of representation of the actual pore space. Generally two methods to reconstruct pore networks are available; Stochastic reconstruction and grain-based reconstruction (Xiong et al., 2016). Usually these methods yield regular lattices.

#### *2.1.2.1. Stochastic reconstruction*

Before modern advancements in 3D imaging, high resolution 2D pore space images were readily available. Using statistical approximations for distributions of different geometrical properties could be used to reconstruct 3D images, using one-point (porosity) and two-point (pore size, shapes) correlation functions (Adler and Thovert, 1998). These functions worked adequately for geometric properties, but failed to replicate the topology of the medium, as this cannot be scaled from 2D-images easily. Liang et al. (2000) incorporated macroscale flow parameters and matched these with the stochastic model. Silin & Patzek (2006) showed the capillary pressure curve in multiphase flow does not depend on macroscale parameters such as porosity or pore size, but rather on local connectivity (coordination numbers) and geometries. However, for scaling pore network processes to larger scales it is important to be able to generate stochastically representative networks. Depending on the objective of the reconstruction different methods perform on different levels (Xiong et al., 2016).

### 2.1.2.2.    Grain-based reconstruction

Grain-based reconstruction of pore networks uses geologically realistic networks, by using pore size distributions and model packing and compaction of the spheres (Bryant & Blunt, 1992). It was the first method that predicted absolute and relative permeabilities, capillary pressure, and the electrical and elastic properties of quarts sandstone (Xiong et al., 2016.)  However, this method only works on media with spherical grains of the same size making it not widely applicable. Bakke & Oren (1997) developed a geological reconstruction method, using grain size distributions obtained from 2D tomography, and modelled compaction and diagenesis. This method gave a good representation of the connectivity and could accurately predic transport properties (Oren & Bakke, 2002). Coelho et al. (1997) demonstrated a method in which non-spherical shaped could also be integrated in the reconstruction technique, enabling it to be applied more generally. The problems with this method is that the geological history of a sample has to be known to model this accurately, carbonate systems with highly irregular grains can not be modelled at all., and the integration  of pore shape and wettability in reconstruction methods are not fully understood (Xiong et al., 2016).

## 2.1.3.   Direct mapping of pore networks

Direct mapping of real samples uses the actual geometry and topology of a sample, yielding an irregular lattice (Piri & Blunt, 2005). These irregular networks are not directly able to be upscaled, but are used to validate physical assumptions for flow simulations, by comparing the model with experimental data or other modeling methods (Xiong et al., 2016). There are two widely used methods to extract pore networks directly from 3D tomography data; medial axis and maximal ball (Xiong et al., 2016). Recent advances also used a combination of both methods to eliminate problems with either of the methods (Yi et al., 2017).

### 2.1.3.1.    Medial axis

The medial axis method simplifies the pore space into a single voxel skeleton. The skeleton is constructed by either thinning (Baldwin et al., 1996) or pore-space burning (Lindquist et al., 1996). The medial axis mathematically preserves the topology, but problems arise with identifying pores unambiguously. The boundaries between pore bodies and pore throats are not well defined, but generally pore bodies are nodes, and throats are the local minima along branches connecting the nodes (Jiang et al., 2007). Also multiple junctions occur within one pore (figure 3), and the medial axis is highly sensitive to small irregularities within on the surface (figure 4),  so merging algorithms have to be applied to trim the skeleton and fuse junctions without acquiring unrealistically high coordination numbers (Jiang et al., 2007).
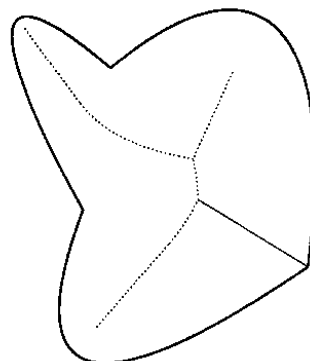


**Figure 3.** *Medial axis of an irregular shape, demonstrating multiple junctions within one pore*.
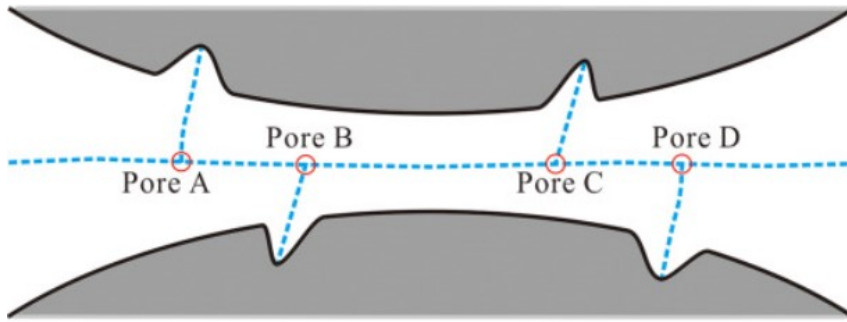
*Figure 4. Pores that occur in the medial axis, due to high sensitivity to irregularities on the surface. Trimming algorithms have to be applied to prevent these from occurring (Yi et al., 2017).*

### 2.1.3.2. Maximal ball

The maximal ball algorithm (Al-Kharusi & Blunt, 2007, Dong & Blunt, 2009, Silin & Patzek, 2006,) uses largest inscribed spheres on each voxel of the pore space. The spheres that are included in other spheres are removed, while the rest are called maximal balls. The maximal ball method uses a different definition of a pore body and a throat as is generally used in the medial axis method. In the maximal ball method a pore body is a larger ball than the surrounding balls, and a throat is a connection between the large balls. The pores do not necessarily have to be a junction between pore bodies.
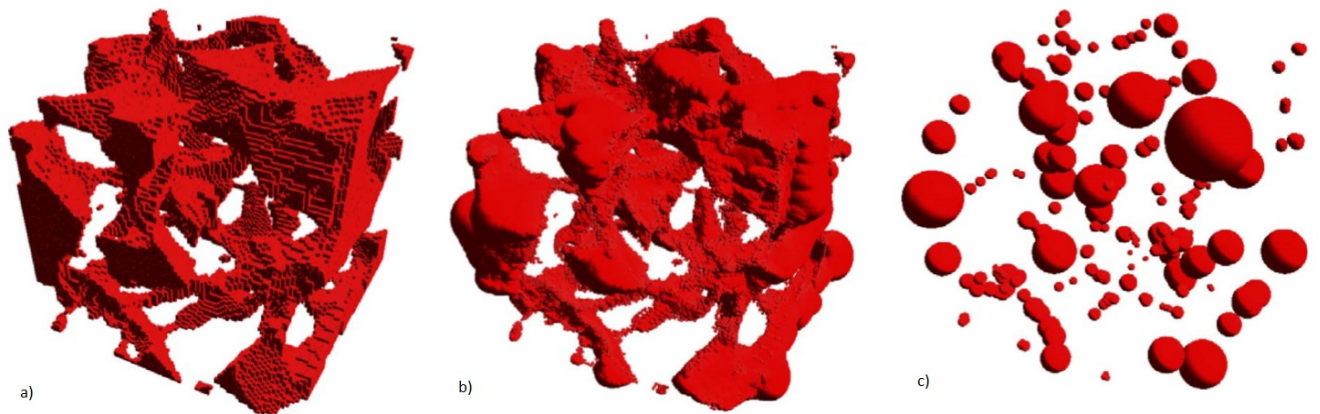


*Figure 5. maximal ball algorithm. A) original porespace b) maximal balls c) The largest balls, defined as pore bodies (Silin & Patzek, 2006).*

While the maximal ball algorithm has a clear distinction between pore bodies and throats, it is computationally demanding, and results in pores with unrealistically high coordination numbers. In addition the throats defined by maximal ball can have a higher tortuosity than in reality (Yi et al., 2017).

### 2.1.3.3. Combined methods

Yi et al. (2017) created an enhanced network extraction model, using a combination of the maximal ball and medial axis. First the medial axis was extracted, and then the maximal ball algorithm was performed on the medial axis voxels only. Irregularities in the pore throats (Figure 4) were eliminated by the maximal ball, as the balls would be smaller than on the throat itself, and only remained if the balls at the end of the side branch were larger than the ones in between. The ancestor balls are defined as pore body, and the balls connecting the ancestors are defined as throats. The remaining pore space is segmented into pore bodies and pore throats using an expansion algorithm, in which the pore body expands in larger steps than the pore throat, so they will contain a larger volume. This model

performed better in terms of permeabilities, relative permeabilities and multiphase flow than the medial axis and maximal ball methods, and the results were closer to the Lattice-Boltzmann method.

The lack of a clear definition of what constitutes pores and pore throats in real porous media with complicated geometries makes it impossible to define which extracted network is more representative for a certain porous medium, as multiple networks can be extracted from the same porous medium (Xiong et al., 2016). The performance can only be validated with experimental data, but different hydraulic parameters have different sensitivities to properties of a pore network. Bhattad et al. (2011) studied the effect of the number of pores per unit volume on transport in porous media. The results showed that single phase permeability is relatively insensitive to pore density. Relative permeabilities are vastly different depending on network structure (Bondino et al.,2013).

## 2.2. Fractures

For the approximation of fluid flow in porous media, fractures are challenging heterogeneities because of its anisotropic nature, as its lateral dimension is much smaller than the other dimensions. The presence of fractures might lead to significant changes in flow behavior in porous media, depending on the scale and aperture of the fracture (Köppel et al., 2019). Fractures can function both as conduit and as barrier for flow, as the fracture can be empty, but also filled with impermeable material, like calcite. Research on fractures is important, as many applications, such as $CO_2$ sequestration, oil recovery, storage of radioactive waste and geothermal energy occur in fault zones and become increasingly relevant topics. Also in porous materials such as glaciers, wood and concrete fractures occur (Berre et al., 2018). Due to the domains in which fractures occur, from millimeters to hundreds of kilometers, pore scale research is a useful tool which can be scaled easily.

### 2.2.1. Flow and solute transport through fractures in non-permeable media

Fractures on large scales in relatively impermeable rocks behave differently than in porous media. On the scale of individual fractures, as opposed to complex fault zones, the fracture is often considered infinite in two dimensions, while having a width in one dimension, called the aperture. Real fractures often oscillate and have locally fluctuating apertures, with significant differences in the aperture over short distances (Berre et al., 2018). In modelling the fracture is often represented by a single average aperture. However, the local aperture fluctuations often cause discontinuities, meaning the average aperture does not represent the actual fracture(Long et al., 1982). In an impermeable medium, the permeability through a plane is given by the Stokes equations, solved for an open channel between infinite planes, is given by the following equation:

$$K_f = \frac{e_h^2}{12} \qquad (5)$$

In which $K_f$ is the fracture permeability[$L^2$] and $e_h$ is the hydraulic aperture[L] (Adler et al., 2012). Eq.(5) shows the cubic relation between aperture and flow. Due to surface roughness of the fracture and partial filling of the fracture, the actual average aperture does not match the aperture that would be calculated using flow and transport simulations. The hydraulic aperture is used for modelling, which is defined as the aperture that matches the flow and transport characteristics of the fracture (Berkowitz, 2002). The definition of the hydraulic aperture is a function of the physical process for which it is needed, as it differs for fluid flow, solute transport and multiphase flow what aperture represents the fracture optimally (Silliman, 1989). Surface roughness has large impact on flow channeling within the fracture. It has been found that 90% of fluid flow can occur through 5-20% of the fracture exit plane (Rasmusien & Neretnieks, 1986) and minor displacements of the fracture walls can change the hydraulic conductivity several orders of magnitude (Durham & Bonner, 1994). As opposed to S-shaped breakthrough curves in homogeneous non-fractured medium, breakthrough

curves measured at exit planes of fractures often have a very fast initial arrival times, with sudden jumps in concentration and long tails, in which diffusion is negligible, even though the scale would suggest that it is not (Becker & Shapiro, 2000).

### 2.2.2. Flow and solute transport models for fractures in porous media

Fractures by itself are complex features, but more problems arise with a fracture in porous material, if the flow through the porous medium is not negligible in the temporal and spatial scale. The pressure distribution in a medium is altered by the presence of a fracture, as the pressure in a fracture will be lower, so in addition to the original pressure gradient there is also a lateral gradient towards the fracture (Berre et al., 2018).

Depending on the scale, different models can be used to simulate flow through fractured porous media. There is a tradeoff between the accuracy in the representation of the background medium and the accuracy in the representation of the background medium (Berre et al., 2018). Several methods to represent fractures are widely used on different scales.

#### 2.2.2.1. Single continuum models

In single continuum models, the permeability of the porous medium and the permeability of the fracture (Eq. 4) are averaged with relation to the volume of the fracture and the porous medium. The aim is to identify an effective permeability $K_e$ so that:

$$q = \frac{K_e}{\mu}(\Delta p - \rho g) \qquad (6)$$

In which $q$ is the flux [L/T], $K_e$ is the effective permeability [L²], $\mu$ is the dynamic viscosity [L²/T], $p$ is the pressure gradient[M·L·T$^{-2}$], $\rho$ is the density [M/L³] and $g$ is the gravitational acceleration [L/T²], using average values over the domain for the flux, and pressure gradient. This is similar to classical upscaling of heterogeneous media, which arises problems by itself (Gerritsen & Durlofsky, 2005). The hydraulic aperture, orientation, area and surface roughness should be considered when upscaling the fracture to a single continuum model, which causes the results of these kind of models to differ widely. The problems with single continuum models to model fractures arise with scaling, as the permeability per scale is different, and boundary condition specific. More complex problems than single phase steady state flow are not adequately represented (Berre et al., 2018).
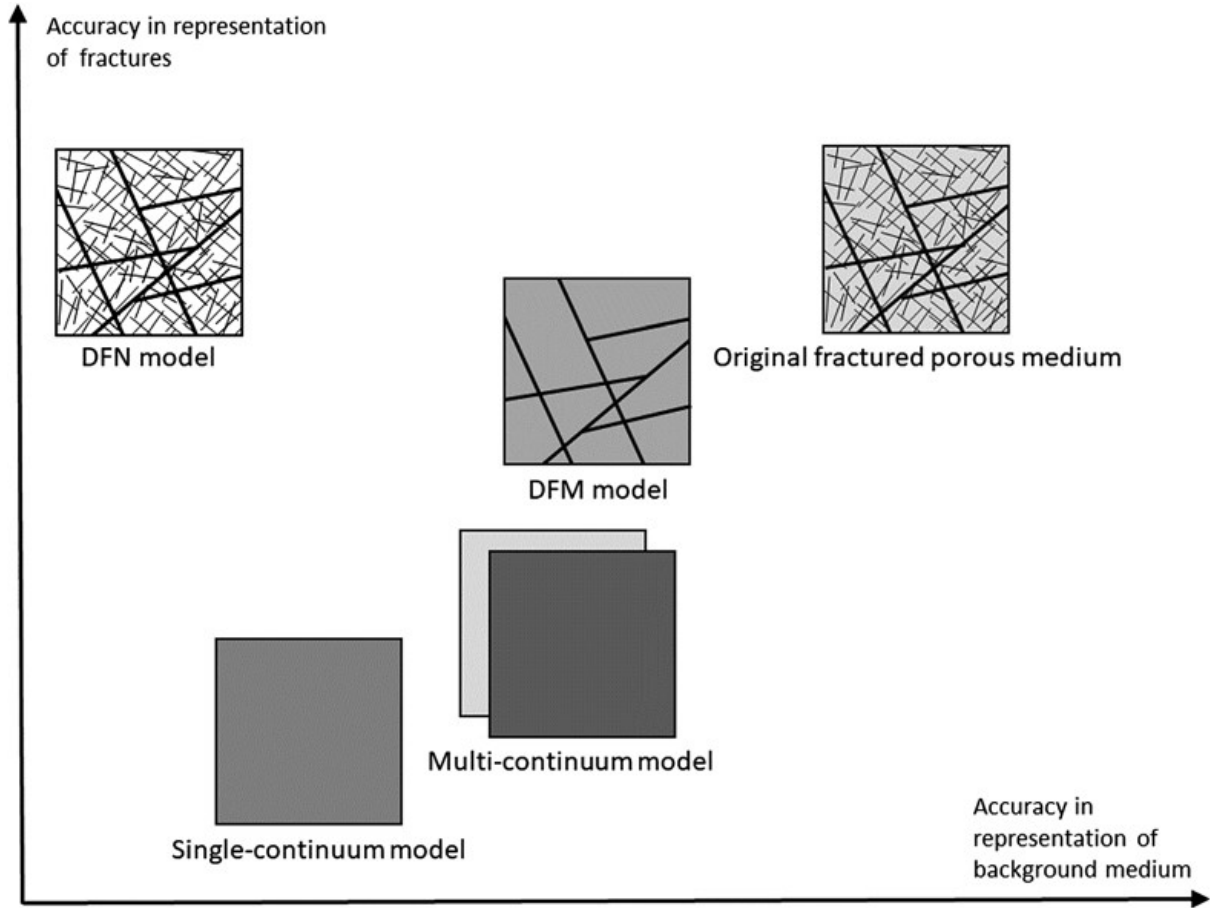
*Figure 6. Different modelling methods in its relation to the accuracy of fracture representation and porous medium representation (Berre et al., 2018)..*

### 2.2.2.2.    Multi-continuum Models

Multi-continuum models represent the fractured porous medium by superimposed media with their own distinctive conservation equations with a transfer term. For continuum $\alpha$, neglecting source and sink terms:

$$\frac{\partial(\phi_\alpha \rho_\alpha)}{\partial t} + \nabla \cdot (\rho_\alpha q_\alpha) = T\alpha \qquad (7)$$

In which $\phi$ is the porosity[-], and $T\alpha$ is the transfer term [M·T$^{-1}$·L$^{-3}$] (Berre et al., 2018). The simplest approach assumes a fracture continuum and a matrix continuum. In that case:

$$T_{Fracture} = -T_{Matrix} \quad (8)$$

The actual value of T is dependent on geometrical, topological and physical properties of the individual continua. The first explicit form was proposed by Warren and Root(1963):

$$T = \sigma\beta(p_{matrix} - p_{fracture}) \ (9)$$

In which $\sigma$ is a factor related to matrix fracture interface area and characteristic length, and $\beta$ is a factor related to physical properties, such as matrix and fracture permeability and fluid viscosity. This equation accurately represents transfer in simple, symmetric geometries with low pressure differences. In more complex systems with nonlinear pressure gradients the transfer function is hard to determine, making the method inaccurate. In addition to the upscaling problems that arise for the

11

individual continua, it is hard to implement the method in an accurate manner for more complex systems (Berre et al., 2018).

### 2.2.2.3. *Discrete Fracture Matrix Models*

As continuum models rely on upscaling methods of both the fracture and the medium, discrete fracture matrix models (DFM) have explicitly represented fractures within a porous medium with a secondary permeability (Berre et al., 2018). The DFM models are mainly used for fractures with significant impact on the flow and transport in the domain. In a fracture network, smaller fractures can still be upscaled and integrated into the matrix to limit computational time. Methods to define which fractures have significant impact and which can be integrated into the matrix are not well defined. Common practice is to base the decision on fracture length (Lee et al., 2001), but more advanced methods exist, which take fracture volume and connectivity into account (Berre et al., 2018).

### 2.2.2.4. *Discrete Fracture Network models*

If a fracture network is located in a relatively impermeable host medium, causing the porosity and permeability to be defined completely by the fractures, discrete fracture network models are used to model the flow and solute or reactive transport in the fracture network. The discrete fracture network models neglects the flow and transport properties within the medium and simplifies the fractures to pipes. This method is mainly used for complicated networks of fractures (Berre et al., 2018).

### 2.2.3. Pore network modelling of fractures

Considering the heterogeneity and scaling problems of fracture modelling, pore network modelling is a decent method, as it represents the porous medium very well, while also able to represent the fractures very well, which is a challenge for many other methods. The first models represented fractures as large pores with high connectivity, neglecting the fracture heterogeneity (Warren & Root, 1963). These seemed not representative, as the heterogeneity and preferential flow paths within a fracture have a large influence on the flow behavior. Hughes and Blunt (1999) approached the fracture as a regular grid of pores and throats for the first time, with locally measured 2D apertures taken into consideration, creating a rough surface with varying permeabilities over the domain. Extracting accurate 3D pore networks from tomography images is more difficult as the resolution in which the apertures are considered has a large influence on the representation of the aperture distribution in the pore network, and additionally the accuracy of the represented fracture (Jiang et al., 2017). Medial axis based extraction methods are not viable for fractures, as the flat plane will be reduced into a line, losing a lot of the spatial data. Jiang et al. (2017) used a medial surface algorithm initially to maintain the fracture plane, by checking if removing a certain voxel would result in a tunnel. The points on the medial surface with the highest inscribed sphere radii are defined as junctions. These junctions are connected in as many directions in the plane as possible. This creates a grid that represents the fracture in the form of a virtual medial axis, which is able to be extracted from complex heterogeneous fracture systems. Lv et al. (2019) used stochastic fractal data to obtain aperture distributions, to create fractures in initially unfractured tomography images, after which the pore network was extracted using the maximal ball method. The extraction method is questionable to work properly for fractures, which is why new methods have been developed (Jiang et al., 2017, Hughes & Blunt, 1999). However, Lv et al. (2019) did flow simulations with and without fractures and compared the permeabilities. The results showed quadratic increase in permeability with fracture aperture.

## 3. Methods

Two different models are created; The first extracts a pore network from CT-images, to obtain a representative pore network for a certain porous medium. To simulate fractures through the porous medium, a second model is created which generates a fracture with apertures and different clogging levels. After that PoreFlow is used for flow and solute transport simulations and STANMOD is used for numerical solutions to obtain dispersivities from breakthrough curves.

### 3.1 Extraction of the pore network

The best working model for all purposes is by Yi et al., who used the maximal ball algorithm on the medial axis, which compensates for the errors in both methods. The model proposed in this thesis uses a similar approach, but with reduced computational time . To  obtain the pore network with pore properties from CT-images, the sample has to undergo several operations. 1)  It has to be binarized and a skeleton has to be constructed. 2) Pore bodies and pore throats have to be defined. 3)  The shapes and sizes  of the pores have to be obtained. In this study, our method complies with the four considerations that have to be taken into account in network extraction mentioned by Jiang et al.(2007): Topology preservation, single voxel width, medial location and integration of geometry.

#### 3.1.1   Skeletonization of the Sample

The CT image has grayscale values in a small spectrum of the possible values, depending on the sample and the imaging method. To obtain the pore network from CT-images, first the pores and grains have to be defined using binarization of the sample. In order to compare the results with different extraction methods, already segmented images are used.  Floating grain voxels within the pore space could be present, but since these are physically impossible to exist, they are removed using the *3D fill holes* operation provided in the ImageJ package (Ollion et al., 2013).

For the skeletonization of the sample the *Skeletonize3D* and *AnalyzeSkeleton* plugins in ImageJ (Arganda-Carreras et al., 2010) have been used. These plugins use the thinning algorithm developed by Lee et al. in 1994. It focuses on connectivity by eroding the pores from the outside until the width of the remaining pore is only one voxel, while continuously keeping the Euler characteristics constant. This makes it impossible for pores to disconnect, because the moment the pore becomes one voxel wide, it will not be removed anymore, as all sides erode at the same time the medial axis is what remains. This algorithm complies with three of the four beforementioned considerations by Jiang et al.(2007): topology preservation, single voxel width and medial location. This method has been chosen over maximal ball method (Silin & Patzek, 2006), as the computation time of the medial axis is much shorter, and the chance of getting unrealistically high coordination numbers is smaller, which depends on the junction merge algorithm that is used. Yi et al. (2017) used maximal balls to obtain the medial axis, but that is also computationally demanding. A new junction merge algorithm is proposed in paragraph 3.1.2, which prevents unrealistically high coordination numbers, and eliminates the small branches of which the connected pore bodies have overlapping inscribed spheres. *AnalyzeSkeleton* is used to obtain junction locations, end points and the Euclidean and tortuous lengths of the branches.

#### 3.1.2   Defining Pore Body and Pore Throat Locations and Sizes

Several definitions of pore bodies and pore throats exist, but in this study the method by Jiang et al. (2007) is used, which divides the pore space into junctions (pore bodies) and the connection between the junctions (pore throats). Information from the skeletonization algorithm makes this step possible, as junctions are voxels surrounded by more than two voxels and throats (or non-junctions) are points with two connecting voxels. Medial axis thinning could however create multiple junctions within one pore (figure 7) when the shape has irregularities (i.e., several junctions close to each other). Other studies solved this by eliminating short pore throats beneath a threshold value and overlapping pore

throats by using the average location (Bultreys et al., 2015, Jiang et al., 2007, Lindquist et al, 1996) . Eliminating short branches is arbitrary, which is why in this study we use a set algorithm to solve this problem, and find the most representative location of the pore instead of the average of the given locations. A method is needed that does not cause unrealistically high coordination numbers, and resolves overestimations of the amount of pore bodies or overlying pore bodies within one pore. Here, we propose a new method which do not cause problems with either of these situations. The merging algorithm used is similar to the one used in the maximal ball method, in the sense of merging the balls based on inscribed spheres.

3. Define the radius of the maximum inscribed sphere of all junctions using a distance-to-grain-voxel map of the binary images.

4. Create clusters of overlapping maximum inscribed spheres. For example,  if pore 1 would overlap pore 2, and pore 2 overlaps pore  3, but pore 3 does not overlap pore 1, this is still defined as a cluster.

5. Sort the cluster on pore size. The master is defined as the pore body in each cluster with the largest radius (Silin & Patzek, 2006). It is called the master as its position is mostly the most centred in the pore, which is why it is the largest. Its position is the most representative for the pore.

6. Scan over the cluster from largest to smallest pore. If the pore overlaps with the master pore, it becomes a 'slave'. If it does not directly overlap with a master, it becomes a master itself. Using 'a slave of my slave is also my slave' (Silin & Patzek, 2006), slaves overlapping with pores that are defined as slave are also defined as slave, with the same master.

This method only merges all the pore bodies, if the inscribed sphere decreases from the largest outward. If not, multiple pore bodies will remain. As several of the pore bodies within a cluster could remain, unrealistically high coordination numbers and the merging of pores which are essentially in one channel are prevented from occurring. This method keeps the largest pore bodies, as these pore bodies carry most of the flow, while maintaining the geometry of irregularly shaped pores. This method results in more representative pore body locations than earlier proposed methods. Another problem with medial axis network extraction is the high sensitivity to irregularities on the surface of the throat, creating many dead ends, which are not actual separate pores. To make a distinction between actual dead ends and unnecessary dead ends, the inscribed sphere of the throat has to be smaller than the inscribed sphere of the pore. If this is the case, the pore remains, as it will function as a container, and solute can diffuse in and out of it. If this is not the case, it is not defined as pore body, and will be removed. The junction pore connected to the dead end will remain intact, as this will create a higher accuracy if the throat it is located in is heterogeneous. If the throat is not heterogeneous, it will not affect the flow parameters.
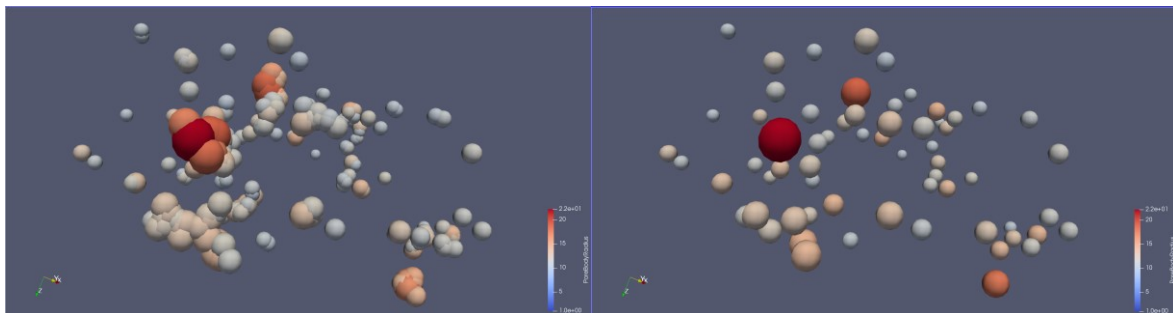


*Figure 7. Pore bodies with radius larger than 10 voxels before and after using the merging algorithm.*

To obtain the pore sizes, watershed segmentation of the pore bodies is used to determine the volume equivalent radius. Watersheds are usually determined with topographic data, by filling up the basin with water, starting from the lowest point until the area is completely covered. Our method uses this theory in 3D. The starting points are specified markers. The topographic map that is needed is created by using the distance map of the pore bodies with its radius, so not only the distance between pore bodies is used, but also the size. This makes the area close to the pore bodies more likely to be covered by this particular pore body. For the segmentation the binary map is used as a mask, so only the pore space is segmented. The pore bodies with its radius are used as markers, so the volume equivalent radii have to be larger than the inscribed sphere radii. The sum of the volumes is equal to the porosity of the sample. At the end of the model, pore throats will be assigned volume, which will be subtracted from the matching pore body volume.

### 3.1.3    Determining throat parameters

The smallest point in a throat is used to determine the shape factor and size of the throat, as this is the bottleneck for the flow. Because the voxels have cubic shapes, the area and perimeter perpendicular to the flow direction are difficult and time consuming to calculate for every direction, so the area and perimeter in the nine diagonal and orthogonal directions shown in figure 8 are used. The area per voxel is either 1 for orthogonal directions, or $\sqrt{2}$ for diagonals (figure 9). The smallest area is likely the closest to perpendicular on the flow direction (Yi et al., 2017). The algorithm starts at the throat location on the skeleton, and scans in horizontal and vertical lines on the plane from the centre, until the solid of the grain is reached. This creates a cross with pore voxels from the centre. All pore voxels that are found with a horizontal scan, will be scanned vertically and vice versa in the next step, until solid voxels are reached. This continues until no new pore voxels are found. This method finds the complete shape of the pore throat. The perimeter is determined by counting neighbouring solid cells for every pore cell.  Since the voxels are cubic, the shape only contains corners of 90°. Jiang et al. (2007) tested several methods to compensate for this in the shape factor, but since it is dependent on the used resolution and the type of sample, there is no reliable method to determine how to compensate for it, without introducing different errors. Corners could be more rounded in reality, but flat faces could be rougher, so it could over- and underestimate the shape factor, depending on the sample. There is no method of determining the compensation from the CT-images without experimental data. Usually for the throat size inscribed spheres are used. However, as the average throat size is often more or less twice the resolution (Yi et al., 2017), this means a large part of the throats will have an inscribed sphere of 1 voxel width. This will mean there is no differentiation in area, as long as the inscribed sphere is the same. Also this is scale dependent, as not in every pore shape the medial axis is exactly in the middle.  To compensate for this, the shape factor is used to determine the inradius based on the shape factor and the area. Using the shape factor, the pore sizes are organized in circles, rectangles and triangles with different angles. The inradius of the defined shapes are defined as follows:

$$R_{circle} = R_{inscribed} \qquad (10)$$

$$R_{square} = 0.5\sqrt{A} \qquad (11)$$

$$R_{triangle} = \frac{A}{0.5*P} \qquad (12)$$

As the area is used, which is not scale dependent, instead of only the inscribed sphere, which has large errors for small pores, the inradius gives a scale independent radius for small pores. As the error on the shape factor grows larger for large pores (Jiang et al., 2007), for larger pores the inscribed sphere is used, as the error decreases for larger spheres.
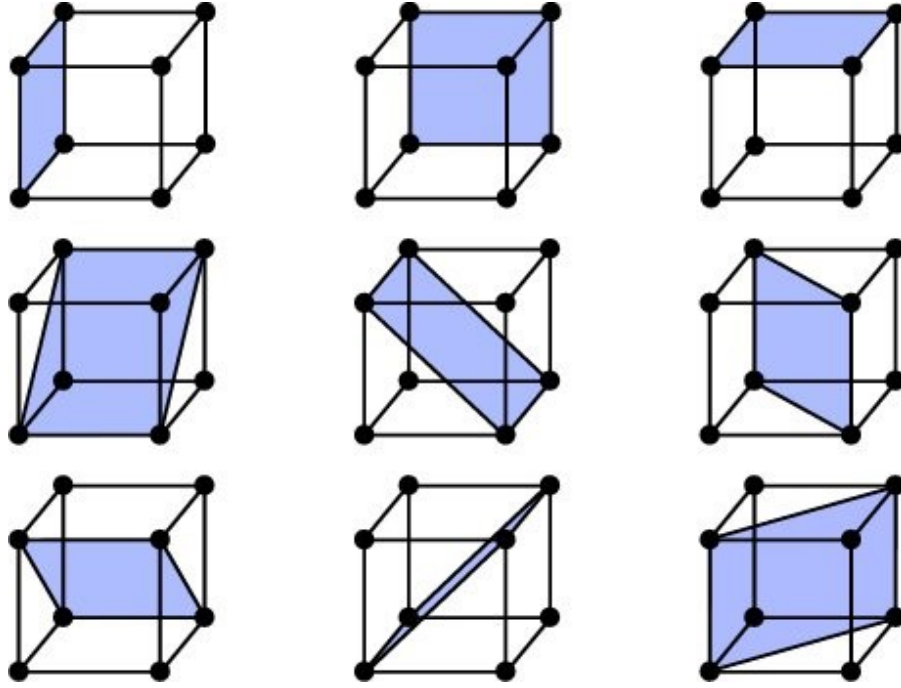
*Figure 8. The nine directions of the planes that are used to find the shape factor.*
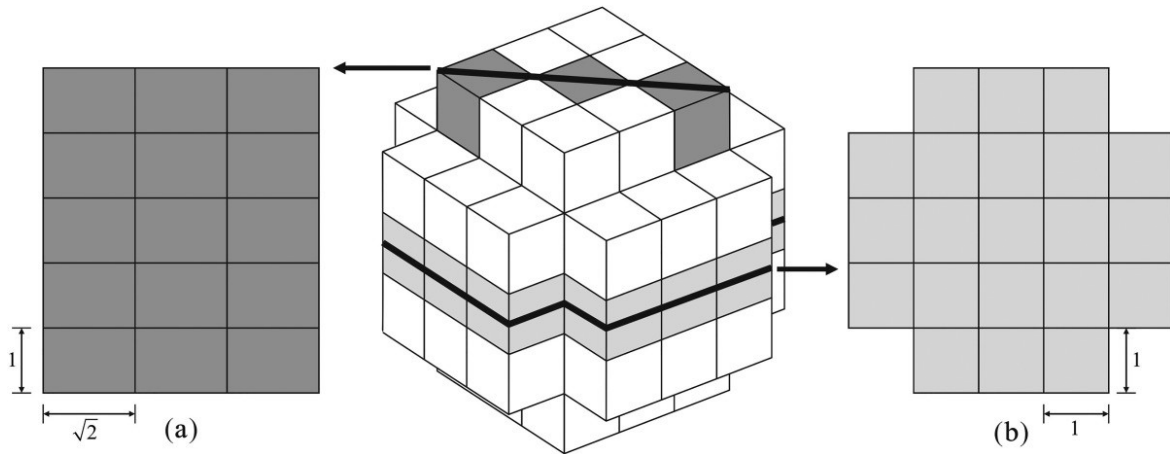


*Figure 9. Cross sections of (a) diagonal cross section and (b) orthogonal cross section used to determine the shape factor (Yi et al., 2017).*

The length of the pore throats depends on tortuosity, and on the boundary between the pore body and throat. As the tortuosity is overestimated by the medial axis, because the medial axis is in the middle, but the actual flowpath cuts corners, and the discretization, an algorithm has to be used to compensate. Yi et al. (2017) proposed a method that uses the aspect ratio (ratio between the pore size and throat size) to determine the length of the throat. This means the throat is simplified to linear pore walls from the pore to the throat location, and simplifying that shape to a rectangle with a single length. The new length is defined as follows;

$$L = L_1 \frac{1 + k_1 + k_1^2}{3k_1^3} + L_2 \frac{1 + k_2 + k_2^2}{3k_2^3} \qquad (13)$$

In which $L_1$ and $L_2$ are the lengths from the throat location to each pore body minus the inscribed sphere of the pore body with $k = \frac{R_{pore}}{R_{throat}}$ for both sides.

Pore bodies connected by multiple throats will be merged into one throat, with the length of the shortest throat, the throat location in the smallest throat and the shape factor of the added area and perimeter. This area and perimeter will be used to calculate the inradius. The inscribed spheres will be added up.

### 3.1.4   Samples

To validate and compare the output of the model, samples originally used by Dong & Blunt (2009) are used. Yi et al.(2017) used these samples to validate their model and compared it with maximal ball and medial axis methods. The samples used are ten sandstones, and two carbonate rocks.

*Table 1. Properties of the samples used to validate the extraction model.*

|  | Berea | C1 | C2 | S1 | S2 | S3 | S4 | S5 | S6 | S7 | S8 | S9 |
|---|---|---|---|---|---|---|---|---|---|---|---|---|
| Size (voxels) | 400³ | 400³ | 400³ | 300³ | 300³ | 300³ | 300³ | 300³ | 300³ | 300³ | 300³ | 300³ |
| Resolution(μm) | 5.35 | 2.85 | 5.35 | 8.68 | 4.96 | 9.10 | 8.96 | 4.00 | 5.10 | 4.80 | 4.89 | 3.40 |
| Porosity (%) | 19.6 | 23.3 | 16.8 | 14.1 | 24.6 | 16.9 | 17.1 | 21.1 | 24.0 | 24.0 | 34.0 | 22.2 |

The samples are meant to give a complete overview of different samples, with different resolutions, grain sizes, porosities and levels of heterogeneity (Table 2)

*Table 2. Binary images of the samples used.*



Berea



C1



C2



S1



S2



S3

S4



S5



S6



S7



S8



S9
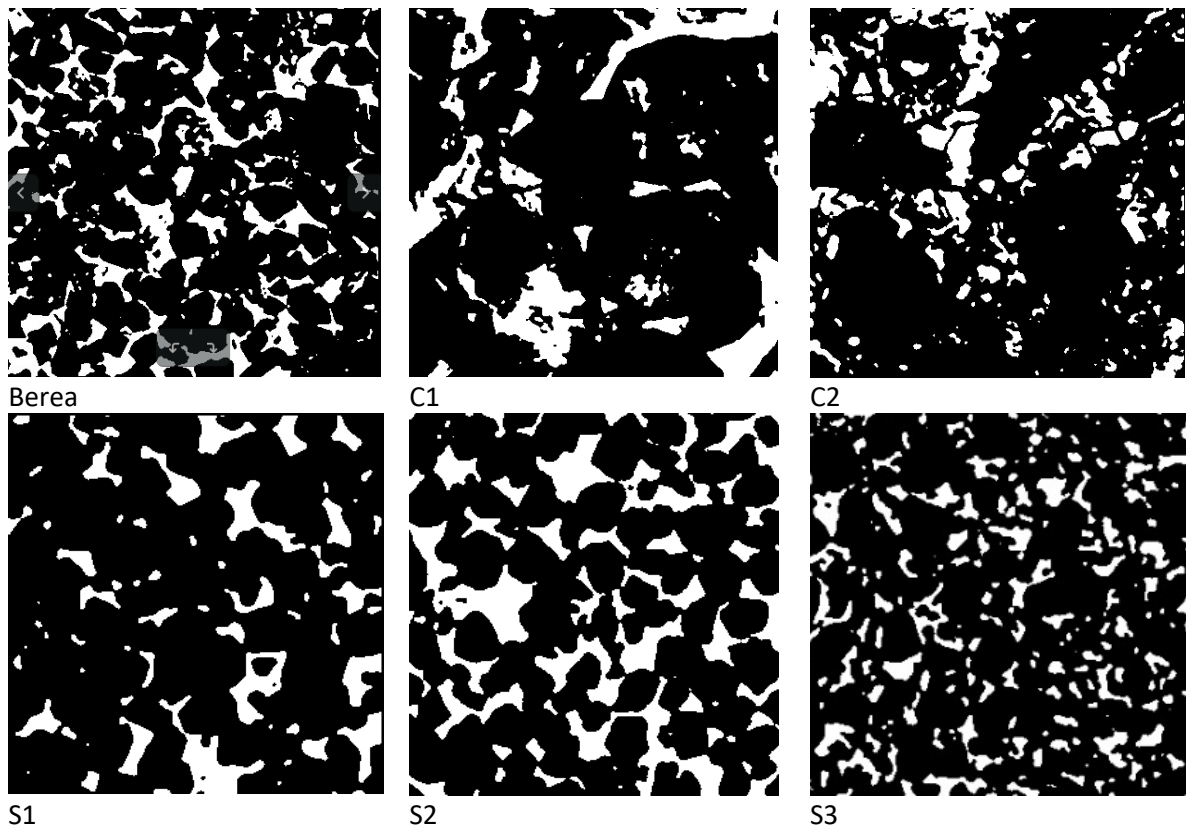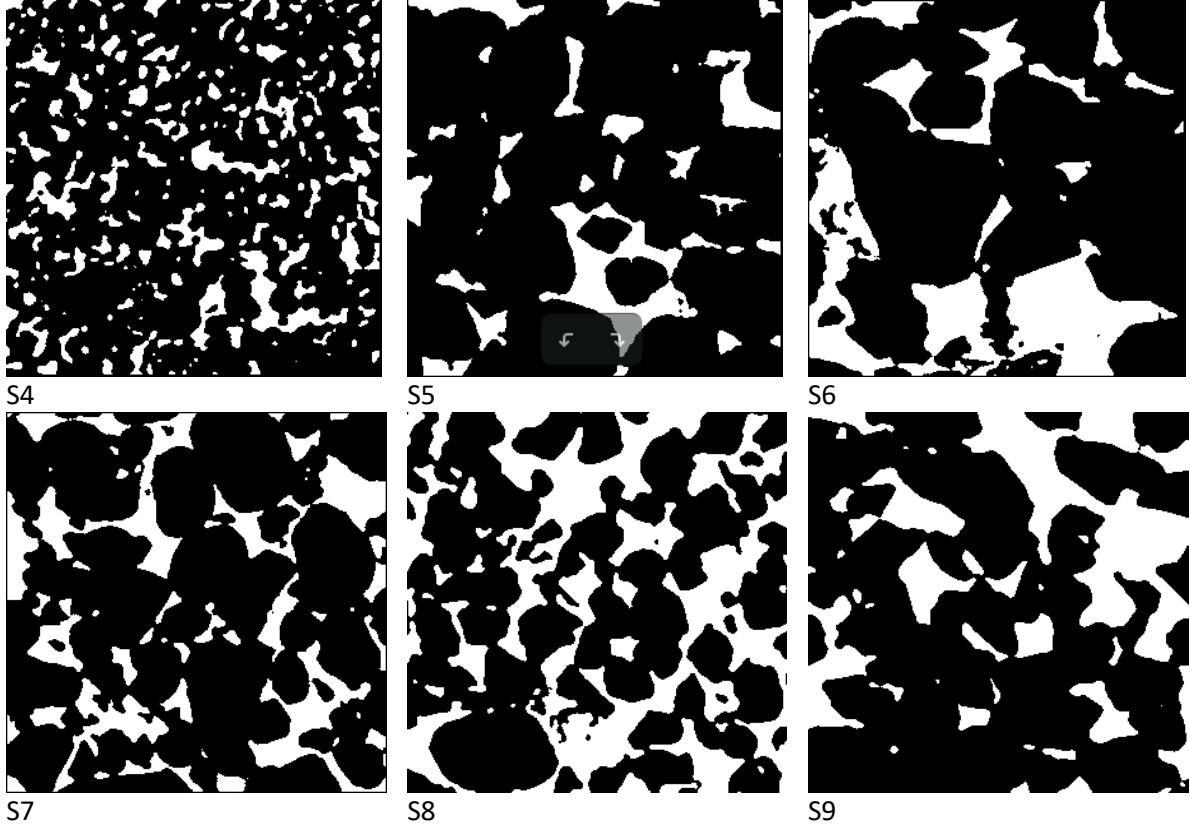
## 3.2 Fracture Model

Given the formulations of pore network modeling, the fracture cannot directly be implemented as a plane in a pore network. To represent a fracture passing through the porous media we have used a regular grid, with parallel and oblique pore throats, connected to all existing pore throats passing through the fracture plane. The regular grid is 25*25 pore bodies, divided over the complete length and width of the sample, through the center of the domain. The hydraulic aperture can be downscaled to a regular grid, while maintaining the conductance of the fracture. The flow through a fracture with a given aperture of $e$ is given by the following equation (Witherspoon et al., 1980):

$$Q_{Fracture} = \frac{\Delta P w e^3}{12 \mu L} \qquad (14)$$

In which $Q$ is the flow rate [L³/T], $P$ is the pressure [M·L·T⁻²], $w$ is the width of the fracture [L], $e$ is the hydraulic aperture [L], $\mu$ is the dynamic viscosity [M·L·T] and $L$ the length of the fracture [L]. The shape of a fracture plane is represented by a regular grid with diagonal connections with cylindrical pipes, in which the flow is parallel:

$$Q_{Fracture} = \sum_{i=1}^{n} Q_i^{parallel} + \sum_{i=1}^{2(n-1)} Q_i^{Oblique} \qquad (15)$$

In which $n$ [-] is the amount of pores in the width of the grid and the flow rate through a pipe is given by the Hagen-Poiseuille equation:

$$Q_{pipe} = \frac{\Delta P \pi R^4}{8 \mu L} \qquad (16)$$

In which $R$ is the radius of the pipe [L] and $L$ the length of a single pipe [L]. These formulations allow easy simulation of a single homogeneous fracture, without taking surface roughness and local heterogeneities into account, with a known hydraulic aperture. Combining Equation 15 and 16 gives:

$$Q_{Fracture} = 25\left(\frac{\Delta P\pi R^4}{8\mu L_1}\right) + 2(25-1)\left(\frac{\Delta P\pi R^4}{8\mu L_2}\right) \quad (17)$$

With

$$L_1 = \frac{L_{total}}{25} \quad (18)$$

And

$$L_1 = \sqrt{\left(\frac{L_{total}}{25}\right)^2 + \left(\frac{w_{total}}{25}\right)^2} \quad (19)$$

as the oblique throats flow diagonally and are longer, causing the pressure gradient to be lower, resulting in a lower flow rate in these throats. Combining equations 14 and 17 and solving for the radius yields:

$$R = \sqrt[4]{\frac{2wb^3}{3\pi(25+48(\frac{L_1}{L_2}))}} \quad (20)$$

The radius R is used for all throats in the regular grid. The fracture plane is placed in the centre of the sample, parallel to the flow direction. All throats that pass through the plane are separated, and instead connected to the closest pore body on the fracture plane. The size, shape and tortuosity of the pores remains intact. Using PoreFlow (Raoof et al., 2013) partially disconnected fracture planes are generated to simulate fracture clogging, in which a fraction of the throats per direction is removed, reducing the connectivity in the fracture and its surrounding pores. The generated planes are from 0% to 70% clogged, as this is the range in which a connected plane can be generated (Table 3). The fracture simulations will be performed on the Berea sample, as it is the size is larger than the representative elementary volume and is relatively homogeneous to limit heterogeneity effects and to be certain the alteration in flow parameters is caused by the fracture.

*Table 3. The different fracture planes used to represent fracture clogging. The clogging fraction increases from 0% (top left) to 70% (bottom right).*
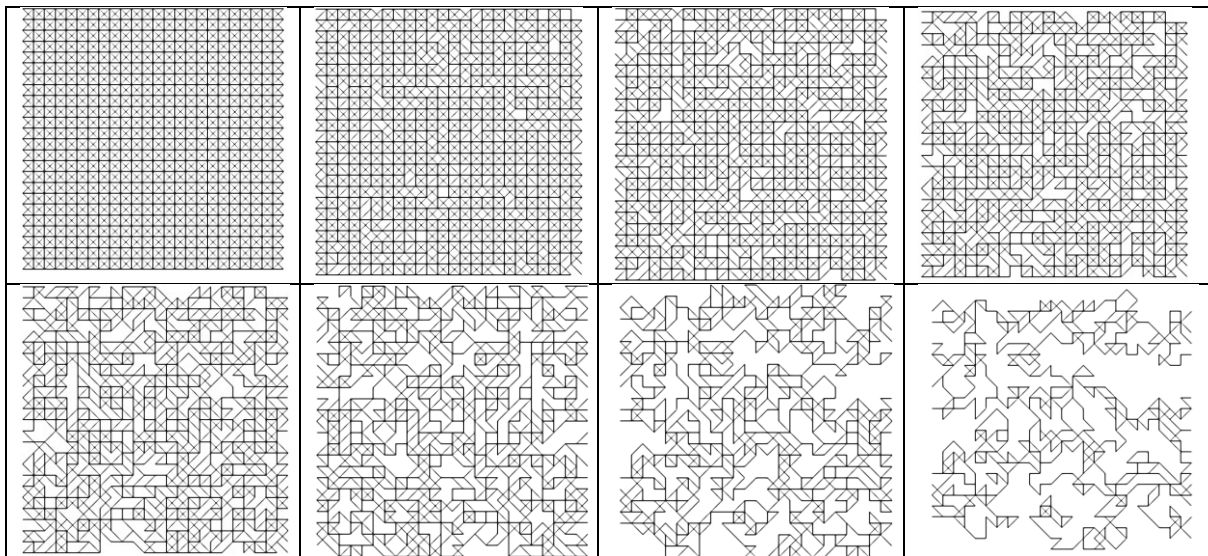
The effect of the increased connectivity by creating a fracture can be obtained by comparing the weighted average of the permeability of the fracture (Eq. 5) and the permeability of the original sample as follows (Cardwell & Parsons, 1944):

$$K_{expected} = \frac{K_{Fracture}*e_h + K_{Sample}*(L-e_h)}{L} \qquad (21)$$

In which K is the permeability, $e_h$ the hydraulic aperture, and L the aperture. With the increased connectivity of the sample the result of Eq. (9) should be less than the modelled result.

### 3.3 PoreFlow

The generated networks are used as input in PoreFlow to run flow, two-phase and solute transport simulations, and is used to obtain flow and transport properties of the network (Raoof et al., 2013). PoreFlow uses cubical pore bodies, and uses shape factors to assign either circular, rectangular or triangular shapes to the pore throats. The Hagen Poiseuille equation is solved for all corners of the throats individually and are then summed. This way the wetting phase is able to flow along the corners, while the non-wetting phase resides in the centre of the pore. In this study PoreFlow is used to validate the extraction model in terms of permeabilities, and to obtain breakthrough curves for the fractured networks. The flow simulations will be performed for three pore volumes, of which the solute is injected for the duration of one pore volume.

### 3.4 STANMOD

STANMOD (Studio of ANalytic MODels, Simunek et al., 1999, van Genuchten et al., 2012) is a software package to evaluate solute transport in porous media using analytical formulations of the advection-dispersion equation:

$$\frac{\partial C}{\partial t} = -v\frac{\partial C}{\partial x} + (\alpha_L v + D_{Mol})\frac{\partial^2 C}{\partial x^2} \qquad (22)$$

In which $C$ is the concentration [M·L$^{-3}$], $t$ is time [T], $v$ is the flow velocity [L·T$^{-1}$], $\alpha_L$ is the longitudinal dispersivity [L], $D_{Mol}$ is molecular diffusion [L$^2$·T$^{-1}$] , and x is distance in the flow direction [L]. As the flow velocity is known from PoreFlow, the equation can be solved for $\alpha_L$.

# 4. Results

## 4.1 Pore network extraction

### 4.1.1 Model parameters

In this section the different statistics for model properties will be discussed for the developed MAMB (Medial Axis Maximal Ball) model, compared with the medial axis method (Jiang et al., 2007, performed by Yi et al., 2017), the maximal ball method (Dong & Blunt, 2009), the axis ball method (Yi et al., 2017).

Table 4 shows the number of pore bodies created by the MAMB model. The MAMB model keeps disconnected pores and has pore bodies with coordination number 2, which the other methods do not. To compare these values for flow properties, these are included. The values are generally slightly larger than the other methods, even without the mid-throat pores considered.

*Table 4. Comparison of number of pore bodies for medial axis (MA), maximall ball (MB), axis ball (AB) and the MAMB methods.*

| Sample | Model | Berea | C1 | C2 | S1 | S2 | S3 | S4 | S5 | S6 | S7 | S8 | S9 |
|---|---|---|---|---|---|---|---|---|---|---|---|---|---|
| Number of pore bodies | MA | 7611 | 4115 | 5590 | 1452 | 2906 | 9104 | 7199 | 659 | 1022 | 1759 | 2439 | 463 |
| | MB | 6298 | 4576 | 8508 | 1868 | 2021 | 8926 | 9556 | 518 | 597 | 1016 | 1324 | 604 |
| | AB | 7283 | 2957 | 4600 | 1857 | 2249 | 8571 | 8433 | 577 | 708 | 1293 | 1603 | 610 |
| All | MAMB | 11930 | 10146 | 15008 | 2493 | 4026 | 13763 | 12761 | 1278 | 1686 | 2407 | 3766 | 838 |
| CN = 0 excluded | MAMB | 10734 | 7898 | 10879 | 2248 | 3774 | 12476 | 10355 | 1078 | 1531 | 2286 | 3103 | 769 |
| CN = 0 and CN = 2 excluded | MAMB | 8637 | 5697 | 8144 | 1681 | 3011 | 9759 | 7629 | 740 | 1102 | 1776 | 2451 | 602 |

The number of pore throats (Table 5) are generally close to the highest number of throats from the MA and MB sample.

*Table 5. Comparison of number of pore throats for medial axis, maximall ball, axis ball and the MAMB methods.*

| Sample | Model | Berea | C1 | C2 | S1 | S2 | S3 | S4 | S5 | S6 | S7 | S8 | S9 |
|---|---|---|---|---|---|---|---|---|---|---|---|---|---|
| Number of pore throats | MA | 14328 | 8893 | 11564 | 2455 | 5792 | 15833 | 11508 | 1243 | 2147 | 3448 | 5235 | 865 |
| | MB | 12545 | 6921 | 10336 | 3048 | 4942 | 15105 | 13322 | 900 | 1234 | 2741 | 4209 | 1054 |
| | AB | 12324 | 4938 | 7093 | 2725 | 4608 | 12911 | 11057 | 899 | 1219 | 2717 | 3820 | 992 |
| | MAMB | 16632 | 12070 | 15664 | 3176 | 6415 | 18621 | 14883 | 1535 | 2407 | 3818 | 5574 | 1137 |
| Throats separated by a pore body with CN = 2 counted as 1 | MAMB | 14535 | 9869 | 12929 | 2608 | 5651 | 15903 | 12156 | 1196 | 1977 | 3308 | 4921 | 969 |

The average coordination number (Table 6) is smaller for the MAMB model than for the other methods, because pores with coordination number 2 exist. If these are not taken into account in the averaging, the values are close to the values in the AB model.

*Table 6. Comparison of average coordination numbers for medial axis, maximall ball, axis ball and the MAMB methods.*

| Sample | Model | Berea | C1 | C2 | S1 | S2 | S3 | S4 | S5 | S6 | S7 | S8 | S9 |
|---|---|---|---|---|---|---|---|---|---|---|---|---|---|
| Average CN | MA | 3,80 | 4,32 | 4,14 | 3,38 | 3,99 | 3,48 | 3,20 | 3,77 | 4,20 | 3,92 | 4,29 | 3,74 |
| | MB | 3,98 | 3,02 | 2,43 | 3,26 | 4,89 | 3,38 | 2,79 | 3,47 | 4,13 | 5,40 | 6,36 | 3,49 |
| | AB | 3.38 | 3.34 | 3.08 | 2.93 | 4.10 | 3.01 | 2.62 | 3.12 | 3.44 | 4.20 | 4.77 | 3.25 |
| CN = 2 included | MAMB | 3,10 | 3,06 | 2,88 | 2,82 | 3,40 | 2,99 | 2,68 | 2,85 | 3,14 | 3,34 | 3,59 | 2,95 |
| CN = 2 excluded | MAMB | 3,37 | 3,46 | 3,18 | 3,10 | 3,75 | 3,26 | 2,92 | 3,23 | 3,59 | 3,73 | 4,02 | 3,22 |
| Max CN | MAMB | 23 | 67 | 63 | 14 | 22 | 29 | 18 | 34 | 41 | 33 | 38 | 21 |

The average pore body radius (Table 7) is larger for the MAMB for every pore body, compared to the other methods.

*Table 7. Comparison of number of average pore body radius for medial axis, maximall ball, axis ball and the MAMB methods.*

| Sample | Model | Berea | C1 | C2 | S1 | S2 | S3 | S4 | S5 | S6 | S7 | S8 | S9 |
|---|---|---|---|---|---|---|---|---|---|---|---|---|---|
| Average pore body radius | MA | 16,79 | 8,66 | 14,62 | 32,59 | 18,05 | 19,92 | 20,90 | 17,84 | 18,79 | 19,01 | 19,82 | 22,03 |
| | MB | 15,36 | 7,05 | 11,39 | 25,59 | 17,25 | 16,69 | 16,80 | 16,71 | 19,00 | 20,15 | 21,16 | 16,20 |
| | AB | 16.65 | 9.78 | 16.26 | 30.12 | 18.83 | 21.38 | 21.84 | 18.18 | 20.89 | 20.03 | 21.91 | 18.30 |
| | MAMB | 25,26 | 12,86 | 18,48 | 50,71 | 27,02 | 32,54 | 32,39 | 25,75 | 31,98 | 28,69 | 23,88 | 30,59 |

The average pore throat radius (Table 8) for the MAMB is generally close to the AB model, which is mostly larger than the MA and MB models.

*Table 8. Comparison of the average pore throat radius for medial axis, maximall ball, axis ball and the MAMB methods.*

| Sample | Model | Berea | C1 | C2 | S1 | S2 | S3 | S4 | S5 | S6 | S7 | S8 | S9 |
|---|---|---|---|---|---|---|---|---|---|---|---|---|---|
| Average throat radius | MA | 9,09 | 4,51 | 7,39 | 16,50 | 9,79 | 10,22 | 10,60 | 9,36 | 9,84 | 10,40 | 11,16 | 10,99 |
| | MB | 7,15 | 4,02 | 6,17 | 12,32 | 8,13 | 7,51 | 7,81 | 9,49 | 10,10 | 9,30 | 10,47 | 8,73 |
| | AB | 9.70 | 5.85 | 9.16 | 16.83 | 10.63 | 11.41 | 11.97 | 11.09 | 12.25 | 11.68 | 12.89 | 10.04 |
| | MAMB | 10,23 | 5,97 | 9,90 | 17,65 | 10,52 | 13,27 | 13,50 | 10,96 | 12,80 | 11,48 | 12,10 | 10,96 |

The throat lengths (Table 9) is about a factor 10 smaller than the other models, for every sample.

*Table 9. Comparison of average throat length for medial axis, maximall ball, axis ball and the MAMB methods.*

| Sample | Model | Berea | C1 | C2 | S1 | S2 | S3 | S4 | S5 | S6 | S7 | S8 | S9 |
|---|---|---|---|---|---|---|---|---|---|---|---|---|---|
| Average throat length | MA | 99 | 82,8 | 100,1 | 204,2 | 103,5 | 117 | 121 | 122,5 | 144,6 | 115,5 | 123 | 132,3 |
| | MB | 143,7 | 88,4 | 122,8 | 232,6 | 154,9 | 161,5 | 151,1 | 187 | 229,2 | 187,3 | 194,4 | 151,2 |
| | AB | 121.2 | 82.8 | 115.6 | 211.3 | 132.6 | 141.9 | 135.6 | 161.3 | 190.6 | 158.2 | 162.2 | 139.4 |
| | MAMB | 11,7 | 7,8 | 12,1 | 20,2 | 11,8 | 14,5 | 14,6 | 12,2 | 15,5 | 14,1 | 17,3 | 10,8 |

### 4.1.2 Performance

The permeability results of the pore network extraction for the different samples is shown in Table 10. As a method such as Lattice Boltzmann considered the real shape of pores, the average relative error is calculated based on the Lattice Boltzmann simulations performed by Yi et al., (2017). The model has the largest error on S3 and S4, which are samples with low resolutions. The error is the lowest for the Berea sandstone.

*Table 10. Permeability results for the network extraction model, compared with different existing models. Yi et al. (2017) and Dong & Blunt (2009) both performed Lattice Boltzmann simulations on the samples, with different results.*

| Samples | Berea | C1 | C2 | S1 | S2 | S3 | S4 | S5 | S6 | S7 | S8 | S9 |
|---|---|---|---|---|---|---|---|---|---|---|---|---|
| $K_x$ | 1796 | 1093 | 200 | 2792 | 3957 | 1507 | 1041 | 3790 | 11813 | 5151 | 9011 | 3035 |
| $K_y$ | 1770 | 2216 | 339 | 3078 | 3659 | 1923 | 1165 | 5201 | 10380 | 6505 | 9591 | 4070 |
| $K_z$ | 1585 | 871 | 215 | 2107 | 3073 | 1233 | 721 | 3932 | 7636 | 4666 | 7992 | 2282 |
| $K_{average}$ | 1717 | 1393 | 251 | 2659 | 3563 | 1554 | 976 | 4308 | 9943 | 5441 | 8865 | 3129 |
| $K_{AB}$ (Yi et al., 2017) | 1790 | 1569 | 188 | 2517 | 4751 | 892 | 541 | 6481 | 13937 | 8813 | 15187 | 2860 |
| $K_{maximal\ ball}$ (Dong & Blunt, 2009) | 1111 | 556 | 158 | 1486 | 3950 | 281 | 169 | 5369 | 11282 | 7926 | 13932 | 3640 |
| $K_{medial\ axis}$ (Yi et al., 2017) | 1790 | 2009 | 263 | 3020 | 4685 | 1325 | 823 | 6384 | 15635 | 7515 | 15092 | 3267 |
| $K_{LB}$ (Yi et al., 2017) | 1777 | 1647 | 206 | 2410 | 4779 | 897 | 528 | 6386 | 15769 | 9068 | 15743 | 2790 |
| $K_{LB}$ (Dong & Blunt, 2009) | 1286 | 1102 | 72 | 1678 | 3898 | 224 | 259 | 4651 | 10974 | 6966 | 13169 | 2224 |
| Error relative to $K_{LB}$ | -3% | -15% | +22% | +10% | +25% | +73% | +85% | -33% | -37% | -40% | -44% | +12% |
| Error relative to $K_{LB}$ | -25% | -21% | -71% | -37% | +9% | -86% | -73% | 8% | 10% | 28% | 49% | -29% |

## 4.2 Fractures

The results of the fractures will be discussed in three sections including the 3D distribution of the modelling domain, the permeability variation of the whole samples and the solute transport parameters.

### 4.2.1 Model observations

The model created a fracture in the centre of the model, as shown in Figure 10. Solute transport simulations are performed for a time period equal to three pore volumes.
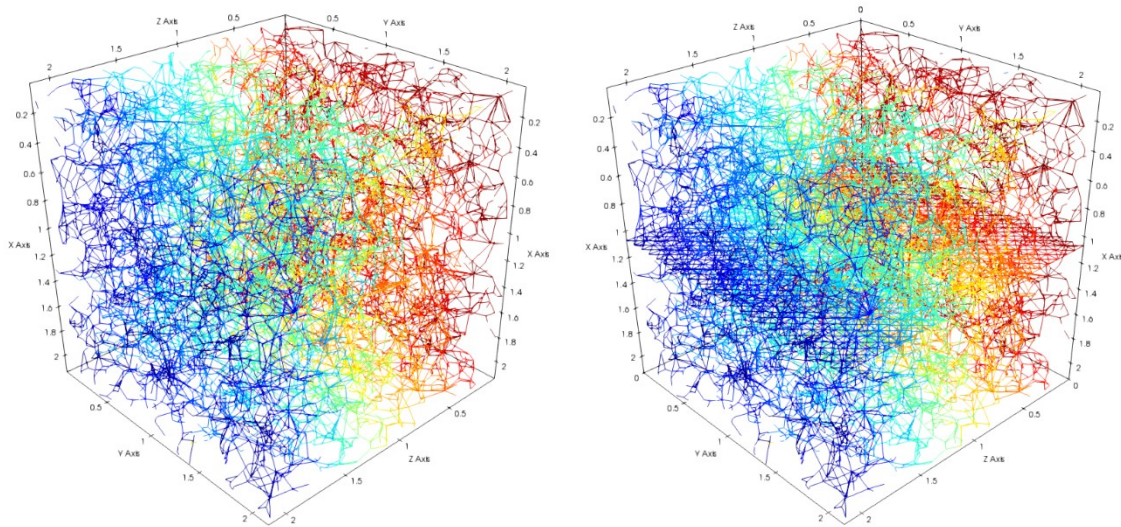


*Figure 10. The Berea Sandstone with and without the modelled fracture.The colours represent the pressure gradient in the sample.*

Figure 11 shows the solute transport simulation through the model. The fracture becomes saturated with a tracer solute very fast, after which the solute transform laterally into the pores close to the fracture plane. This results in a V-shape vertical profile of the solute distribution. In all simulations, after injecting solute, solute-free water is injected to observe the effect of fracture on solute residence time more accurately.
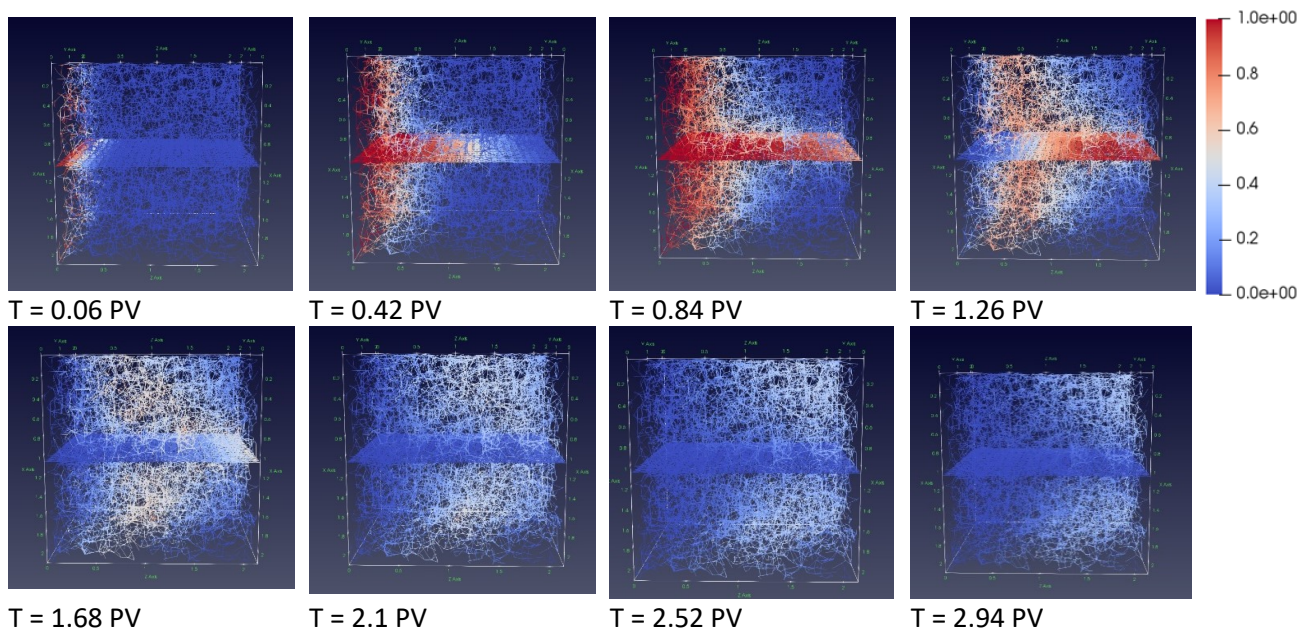
T = 0.06 PV        T = 0.42 PV        T = 0.84 PV        T = 1.26 PV

T = 1.68 PV        T = 2.1 PV         T = 2.52 PV        T = 2.94 PV

*Figure 11. Solute transport simulation through the model with an aperture size of 75µm. The color show the concentration.*

Figure 12 shows the same timestep of the simulations for different apertures. Apertures smaller than 30µm do not show significant difference with the run without fractures. Larger apertures have a higher concentration in the fracture than in the rest of the sample. Also the solute is located increasingly further in the sample with larger apertures.
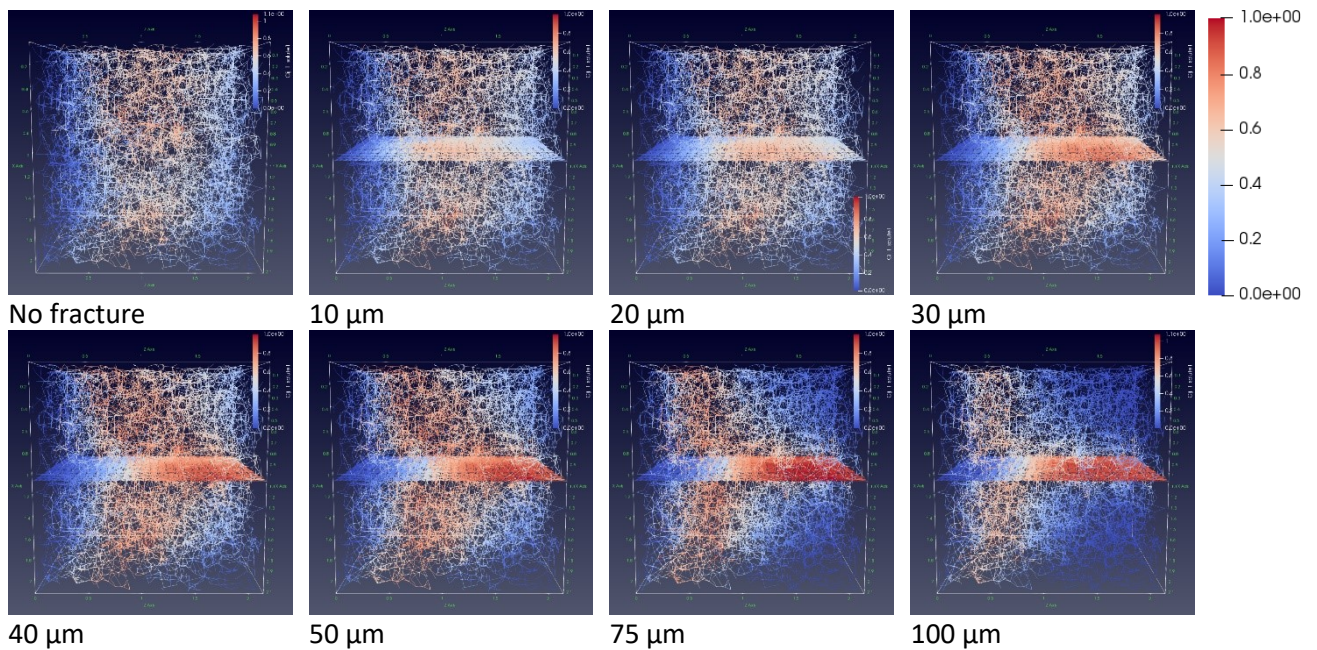


No fracture        10 µm              20 µm              30 µm

40 µm              50 µm              75 µm              100 µm

*Figure 12. Stills of T = 1.24 PV, shortly after the injection stopped, for different apertures.*

Figure 13 shows the effect of the simulated fracture clogging on the solute transport. Clogging causes the solute in the fracture to be less ahead of the solute in the rest of the sample. The concentration gradient perpendicular to the fracture between the fracture and the rest of the sample decreases with increased clogging. Without clogging the solute is distributed uniformly within the fracture . Increased clogging correlates with a more non-uniform distribution of the solute in the fracture.
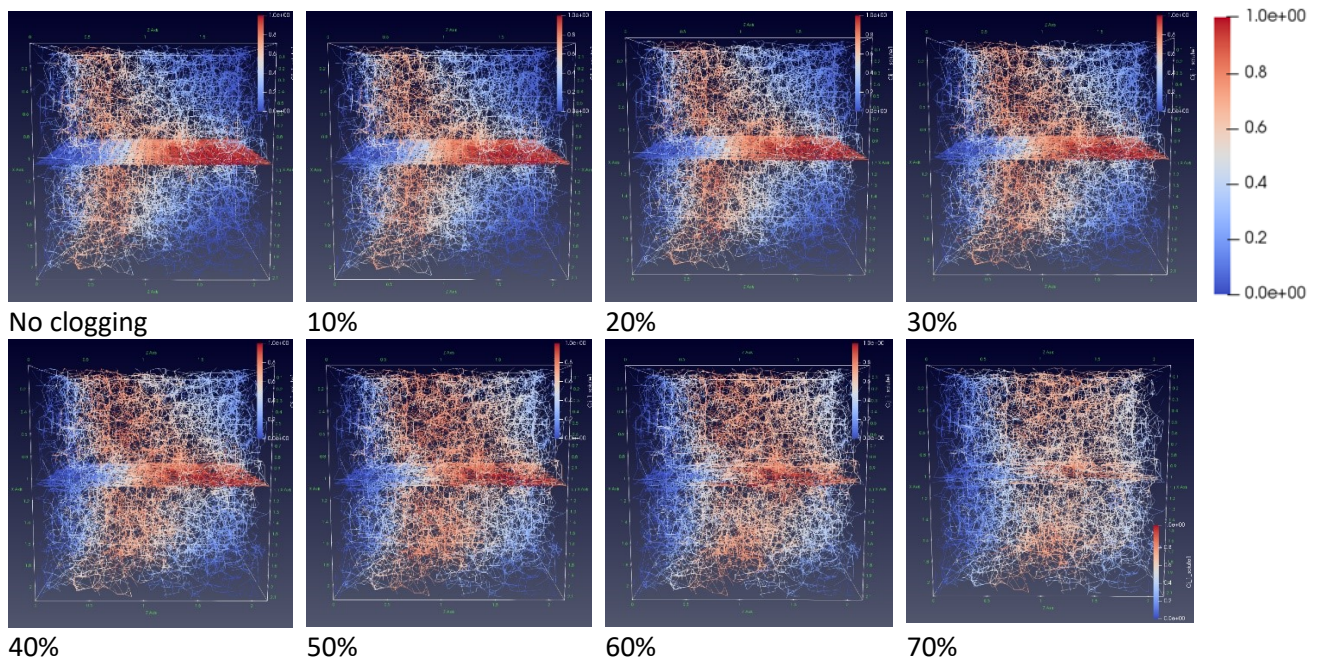
*Figure 13. Stills T = 1.24 PV of the simulation with fracture aperture 75μm, shortly after the injection stops, for different clogging fractions from no clogging (top left) to 70% clogging (bottom right).*

The 70% clogging simulation with 75μm aperture shows similar concentration distributions in side view as the 30μm aperture run with 0% clogging and have similar permeabilities (Figure 15). As the clogging impacts the flow through the fracture in the lateral direction, the top views are compared in Figure 14. The distribution of the solute throughout the sample is more uniform in the non-clogged fracture.
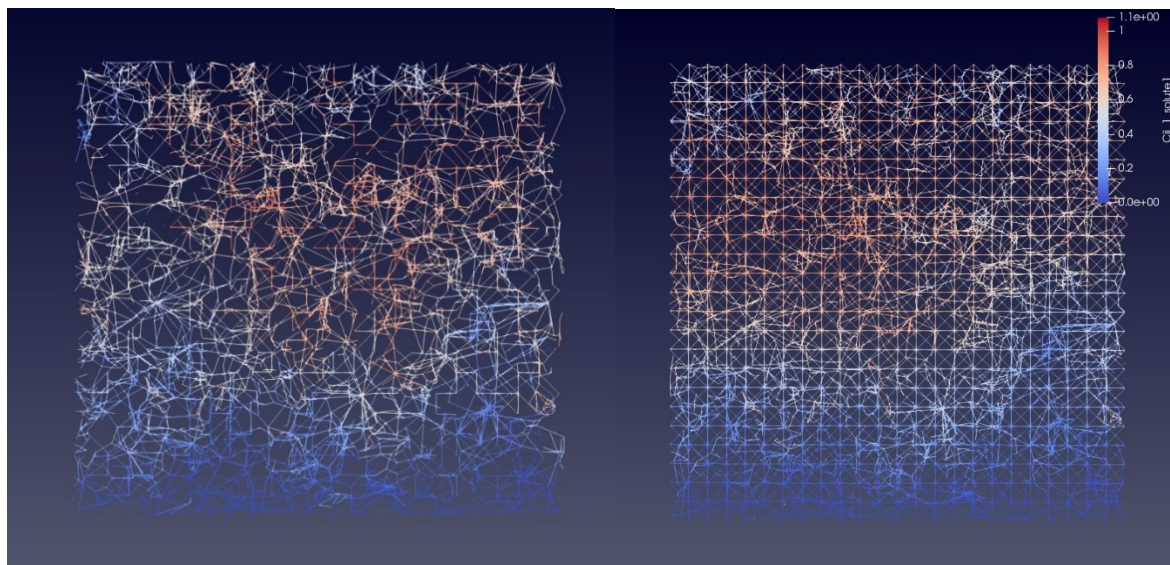


*Figure 14. top view of a slice surrounding the fracture of the sample with aperture 75μm and 70% clogging compared to the sample with aperture 30 μm with no clogging for T = 1.24 PV*

### 4.2.2 Permeability

The Berea sandstone without fractures has a permeability of 1470.7 mD. The permeability results for apertures ranging from 10μm to 100μm are shown in Figure 15. It shows a quadratic increase in permeability for the non-clogged fractions. The permeability decreases linearly per clogging fraction for every aperture.
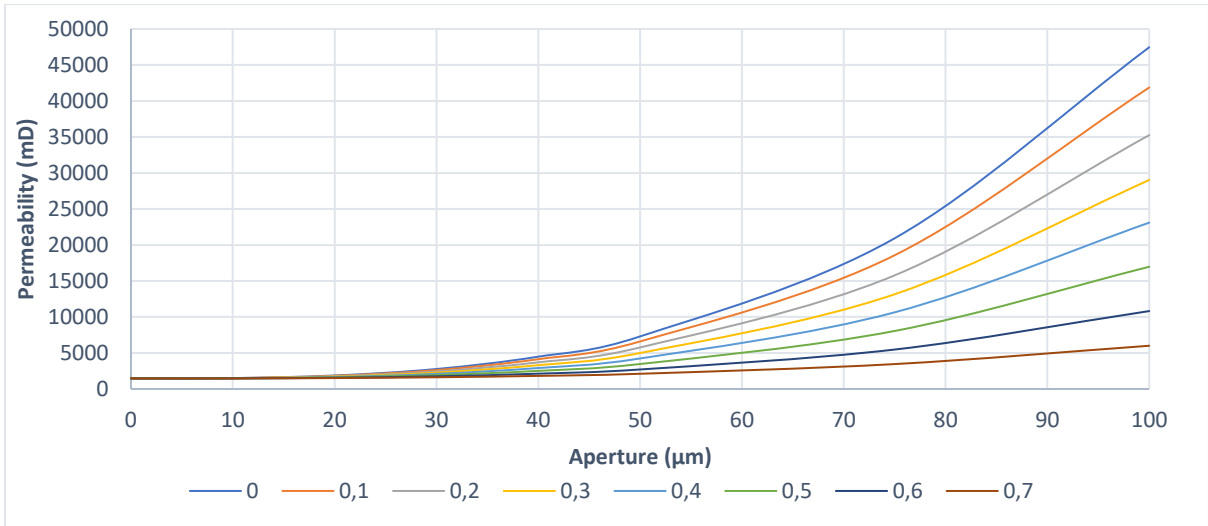
*Figure 15. Permeabilities per fracture aperture in the Berea sandstone for different clogging fractions.*

The modelled permeabilities are higher than the estimated value from Equation 5, where connectivity increase is not taken into account (Fig. 16). For low apertures the difference is small (.5% for aperture of 10 μm) , but increases for higher apertures (13% for aperture of 100 μm) (Figure 17). The curve flattens out at 14%.
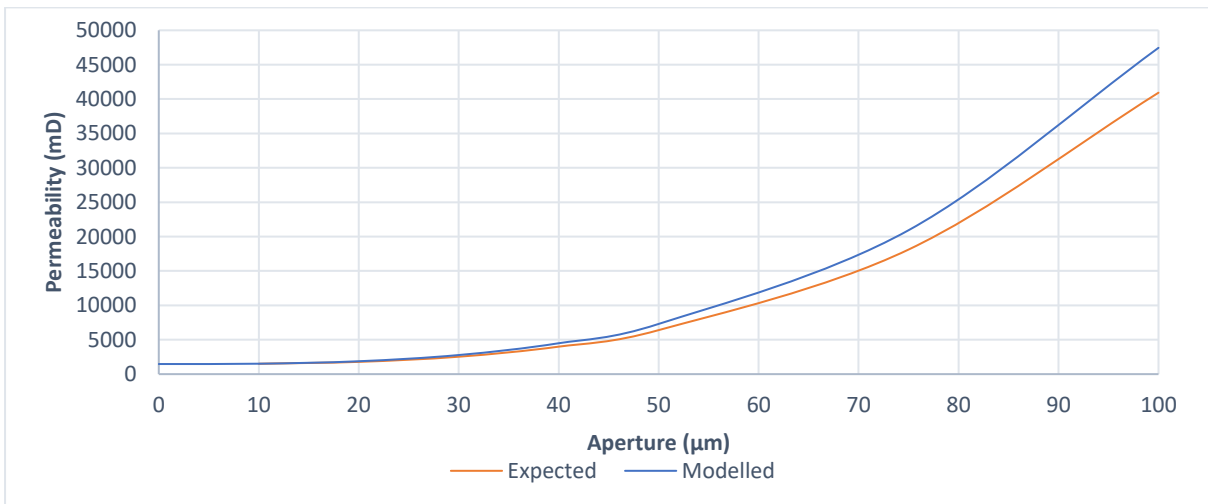


*Figure 16. Expected minimum permeability compared to the modelled permeability.*
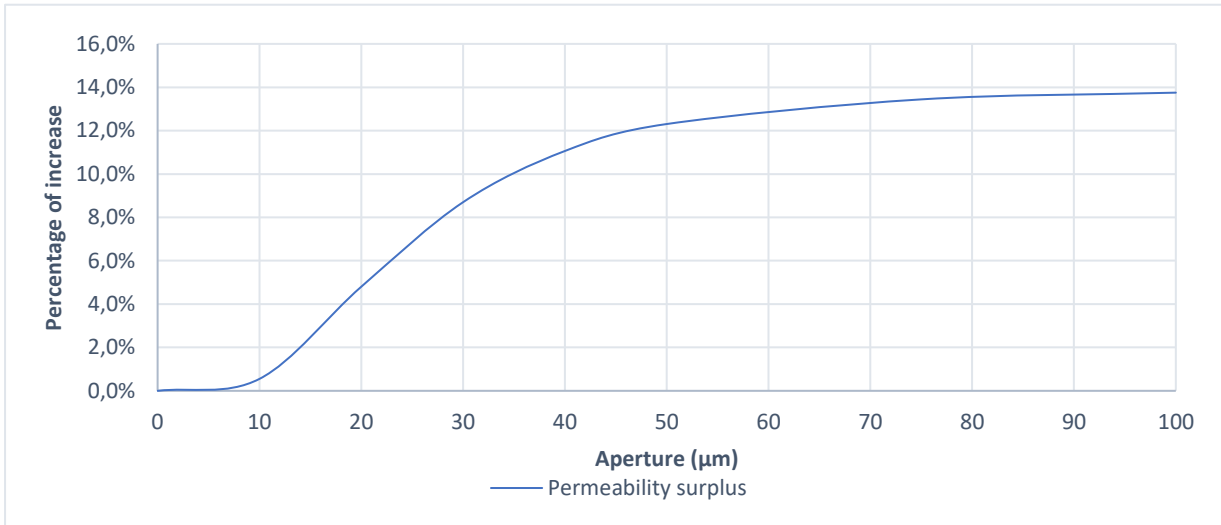
*Figure 17. The increase in permeability due to increased connectivity per fracture plane.*

### 3.1.1   Solute transport

The breakthrough curves for different apertures are shown in Figures 18 and 19. The breakthrough curve for the sample without the effect of the fracture is relatively wide and symmetric. However, in the presence of fractures, with increasing aperture, the breakthroughs become progressively skewed with a strong tailing. Figure 19 shows that the peak concentration becomes wider, arriving earlier than the peak of the non-fractured curve if measured in pore volume. The change in the shape of the curve becomes significant for a fracture aperture of 50 µm or more for this sample.
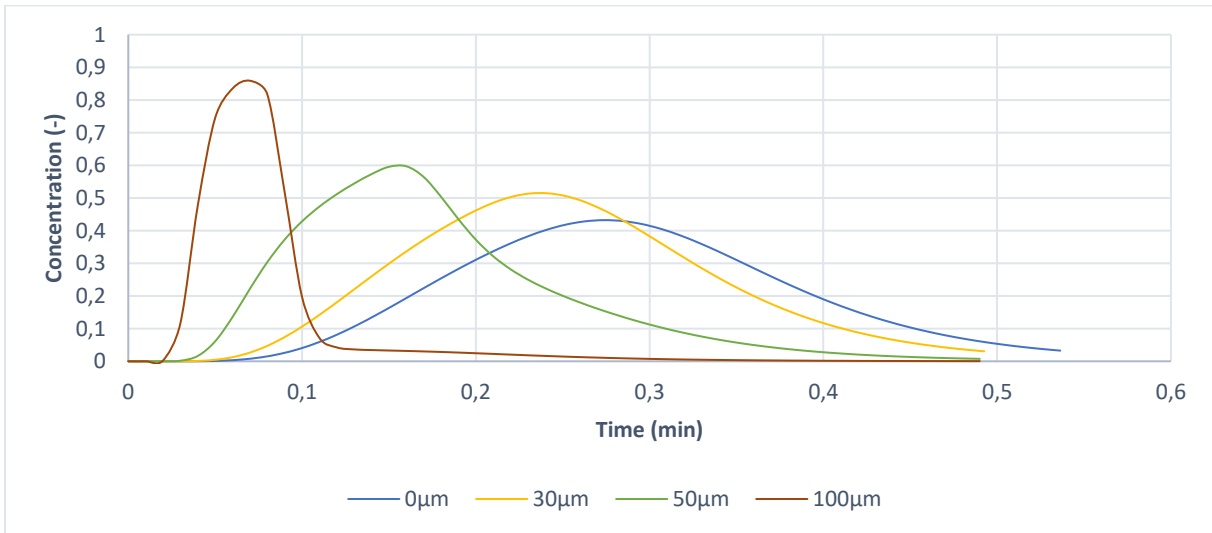


*Figure 18. Breakthrough curves for different apertures, plotted over absolute time.*

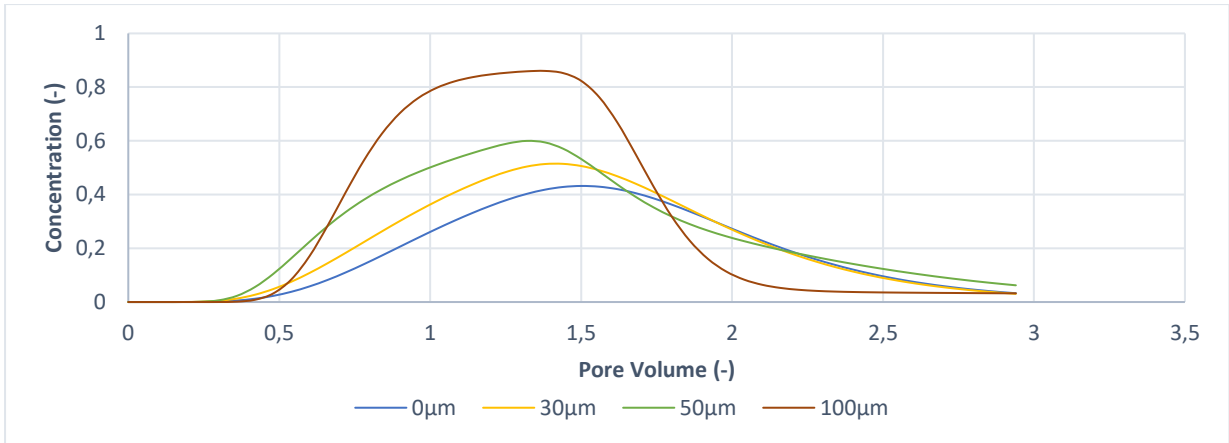Figure 19. Breakthrough curves over pore volume for different aperture sizes, plotted over pore volume.

The breakthrough curves for clogging fractions are shown in Figure 20. It shows the skewness and tailing decrease with increased clogging of the fracture. With a 50% clogged fracture the asymmetry of the curve is still visible.
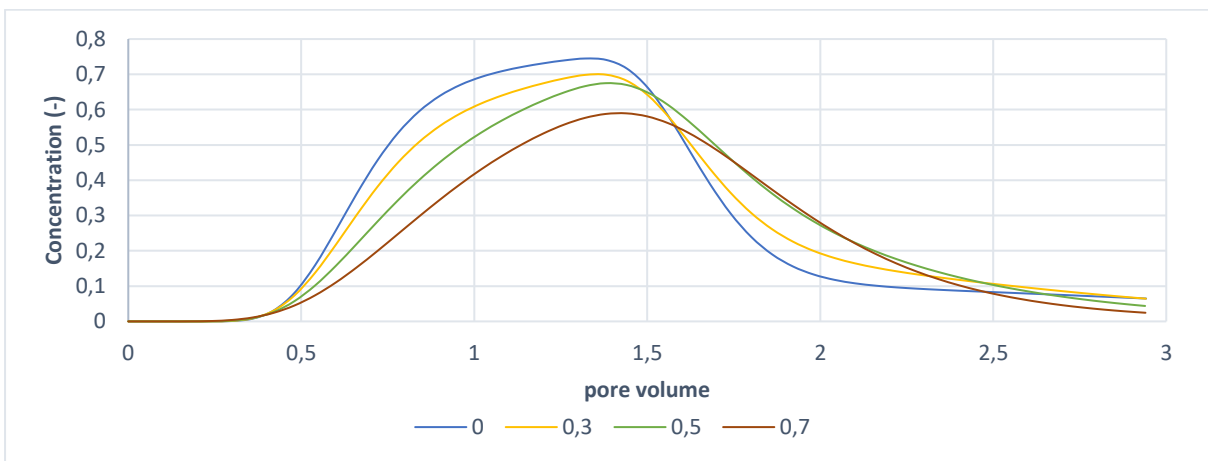


Figure 20. Breakthrough curves for an aperture of 75µm for different fractions of clogging.

The dispersivity values fitted with STANMOD are shown in Figure 21. The Berea sandstone without fracture has a dispersivity of 0.166mm. Small apertures do not impact the dispersivity. For apertures between 30µm and 70µm the values are increased for low clogging fractures, with the maximum values at 45µm. Apertures larger than 70 µm have a lower dispersivity value than the original sample and continue decreasing. Heavily clogged fractures vary less, are generally closer to the original dispersivity value and are lower than the original dispersivity for higher apertures.
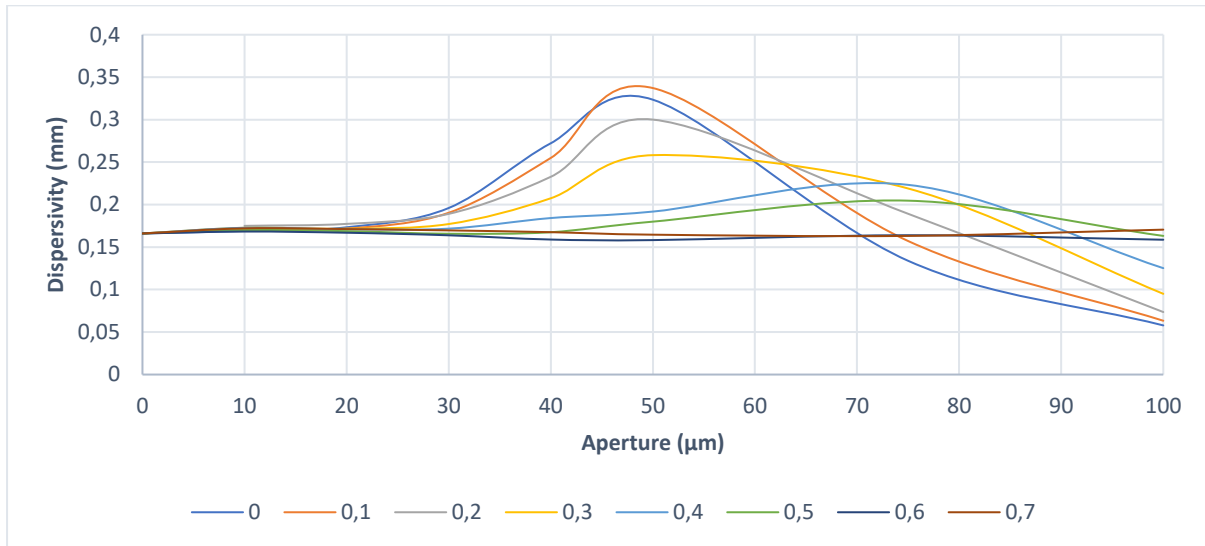


*Figure 21. Dispersivity values for different clogging fractions.*

# 4. Discussion

## 4.1 Pore network extraction

### 4.1.1 Model parameters

Generally the model parameters are comparable with the medial axis, maximal ball and the axis ball methods.

The number of pore bodies is for every sample higher than the medial axis method, even though in basis the concept of the MAMB and the medial axis are similar. The same skeletonization algorithm is used, and a similar definition of pore bodies and throats is used. The difference lies in the merging of the junctions and the removal of dead end pores. The medial axis method merges all overlapping pore bodies into one pore. The MAMB model creates multiple pore bodies between pore bodies if there is a location with resistance. Also the medial axis method removes dead ends based on length, which does not make sense for solute transport, as solutes can diffuse in and out of the dead ends, even if they are shorter than a certain length. The dead end removal used in MAMB is not directly related to just the length, but the length in relation to the pore sizes it is connected to. This works in a similar manner the maximal ball method and the axis ball method solve the problem of getting too many dead end pores. The number of pore bodies in the maximal ball method and axis ball method is based on another definition of pore bodies based on local maxima. This causes an increase in pore bodies for porous media with heterogeneous pore sizes, causing the number of pore bodies to be higher than the medial axis for carbonates, but lower for the more heterogeneous sandstones.

The number of pore throats is directly related to the amount of pore bodies, making it more difficult to compare connectivity between the methods. The MAMB has the most pore bodies for most samples, causing it to also have the most throats, as the MAMB has throats between pore bodies at locations that would be considered one pore body in all of the other methods. The amount of pore throats is generally closer to the medial axis than the other methods for this reason.

The average coordination number is inversely related to the amount of throats, which in turn is related to the amount of pore bodies. Both the amount of pore bodies and throats are generally higher in the MAMB, causing the average coordination number to be lower. The maximal ball method axis ball and the MAMB methods are able to have coordination numbers of 2, while the medial axis does not, causing the average coordination number to be deceiving. A challenge with pore network extraction is preventing unrealistically high coordination numbers. The threshold for an unrealistic coordination number is not well defined, and dependent on the type of sample. The maximum coordination numbers using the MAMB are the highest for the carbonate rocks, which are very heterogeneous, making high coordination numbers possible.

The pore body radii are higher in the MAMB than the radii in any of the other methods. This is caused by the fact that the MAMB uses volume equivalent spheres as sizes, and the other methods use inscribed spheres. If the pore bodies are considered liquid holding containers where the resistance to flow is not present, the volume matters more than the pore body inscribed sphere. In addition the inscribed sphere is resolution dependent, and dependent on how well the medial axis is defined. Defining pores as junctions also causes the pore body locations to not have the maximum inscribed sphere for the pore it is located in. Using watershed to assign volumes to the pore bodies solves this problem. As the pore bodies are not considered to impact the resistance on the flow, the inscribed sphere has no physical meaning.

Using the inscribed sphere for pore throat radii also suffers from high sensitivity to resolution and the location of the medial axis. As the average throat radius is about twice the resolution, this means many

pores have an inscribed sphere radius of 1 voxel length. A radius of 1 voxel length can still have many different surface areas and shapes due to discretisation, even though these pore throats would not have the same hydraulic properties. This causes the inscribed sphere to be only viable for larger pores. The axis ball method uses the maximum inscribed spheres as medial axis, which reduces this error somewhat, but the medial axis and the maximal ball method have no method of solving this. The MAMB introduces the inradius, based on the shape factor, the area and the perimeter. This causes inscribed spheres of 1 voxel length to vary between 0.5 and 1.5 voxel length, based on the area, causing increased variation in these pore throats. The problem with the inradius is that a shape has to be assumed for the shape factor. For low shape factors triangles can be assigned with different angles, making the inradius accurate and unique for all shape factors. For higher shape factors is assumed which will yield the same inradius for a range of shape factors. The inradius works very well for low inscribed sphere values, but as the shape factor is scale dependent and causes surface roughness, the inscribed sphere might become larger than the inradius. In these cases the inscribed sphere is more accurate and is used in the MAMB. This resulted in slightly larger throat radii than the axis ball method, the method which can be assumed to have the most accurate throat radii of the three. The advantage of the inradius used in the MAMB is that it is not dependent on the exact position of the medial axis in the pore.

The throat length is highly dependent on the boundary between what is defined as pore and what is defined as pore throat. Also tortuosity on a medial axis is overestimated, causing problems defining a method that works for every pore. Yi et al. (2017) used an aspect ratio in the AB model, to approximate the boundaries of the pore throat location towards the boundaries of the pore body to be linear, and averaged this to a single width. This makes sense, as approximating the pore throat radius for the full length between the pores would underestimate the flow. This can be fixed by either increasing the throat radius, or by decreasing the throat length. In the MAMB model the pore body inscribed sphere radius is not always larger than the throat radius, which is why the volume equivalent radius is used to reduce the length of the throat. The approximation of linear throat sides towards the outer bounds of the volume equivalent radius is not physical, but it gives a single definition of the boundary between a pore body and a throat. This boundary would be located more into the pore than would be expected if using inscribed spheres, but yields decent results in flow simulations. The lengths of the MAMB are much shorter than the other methods, but the average is influenced by the amount of pore bodies and throats, and by pore bodies within throats with coordination number 2, making the averages difficult to compare.

In total, the MAMB is a method that uses a medial axis and defines junctions as pore bodies, but applies many techniques used in the maximal ball and axis ball methods to solve problems that medial axis had. Also the problems maximal ball had, like too long throat lengths (Yi et al.,2017), unrealistically high coordination numbers, and no clear definition of pore bodies and throats are solved in the MAMB model. A large improvement is the fact that the MAMB model only uses the medial axis to define pore body and throat locations, but for every other aspect of the extraction it is dependent on these locations, and not on the location of the medial axis, which hugely affect the inscribed sphere values for certain locations. Also the MAMB takes into account network parameters that influence solute transport, in addition to flow and multiphase flow, which is the objective of network extraction in many studies.

### 4.1.2  Performance

Important to note when evaluating permeability performance is the fact that the maximal ball and medial axis method have certain parameters that can be calibrated for different samples, such as the smallest size a pore body can have to be defined as pore for the former, and the length of dead end

pores to be removed for the latter. The maximal ball method is originally calibrated to different values than the AB method (Table 9) as different Lattice Boltzmann simulations have been used that yielded different results. This makes the results of the maximal ball method underestimate the values compared to the axis ball method. What the reason of this large difference in results between the Lattice Boltzmann simulations is , is unclear as the authors of both articles do not go into detail about these simulations. This makes it difficult to review the performance of the different models, since the different in Lattice Boltzmann is a factor 4 for some samples. For this study it is assumed the simulation by Yi et al. (2017) is better, as it is carried out more recently.

Another point to consider is the flow simulations through the model are not carried out with the same Navier-Stokes solver, which might impact the way shape factors are implemented, pore bodies behave and boundary conditions of the model are approached. These factors all impact the permeability results.

The permeabilities between all methods are very similar for homogeneous sandstones such as the Berea, S1, S2 and S9. For S3 and S4, there is a lot of spread, as these samples have low resolutions, resulting in many small pores and more discretization problems. This causes the medial axis method and the MAMB method to have much higher values than the maximal ball method. The axis ball method is in between, closer to the Lattice Boltzmann value. The problem could be caused by the skeletonization algorithm used, which is known to have large errors with low resolutions (Jiang et al., 2007). The relevance and importance of performance on low resolution samples is limited, as ultimately the level of representation of the actual rock is the main objective, and low resolution images are less representative of the actual rock.

Samples S5, S6, S7 and S8 consists of relatively coarse grains, with large pores in between, with high porosities and high permeabilities.  The samples consist of a relative small amount of pores. The MAMB method underestimates these values compared to the other methods. There is no clear reason for the underestimation of these samples. The errors might also be due to the fact that the error of the shape factor increases with larger pores, causing the model to have more resistance than it should. In addition, errors in large pores have more impact than errors in small pores on the permeability. This is even more increased if there is only a small amount of pores in the sample to compensate.

Carbonate rocks are very heterogeneous in grain shape and size. This causes problems for the medial axis method, as it will create many dead ends and junctions due to its sensitivity to irregularities. The maximal ball method defines junctions often as pore bodies in sandstone, as these will have larger inscribed spheres. In carbonate rocks this is not necessarily the case, causing errors in the definition of pore bodies, resulting in unrealistically high coordination numbers. The AB and the MAMB have efficient solutions for both these problems, resulting in decent permeability values for both samples.

The samples the model has been tested on are varying in rock type, size, grain size and resolution to test the limits of the models. The MAMB obtains good results for large samples with average porosities and carbonates. These are also the rocks for which it is the most functional, as pore network models are used for samples that are too large to efficiently run with Lattice Boltzmann simulations. With a different approach and definition of pore bodies and throats than the axis ball method, it is also possible to obtain good results, even with the medial axis algorithm by Lee et al. (2009), even though Yi et al. (2017) suggest the results could be improved.

### 4.1.3   Future research

Pore network extraction models have always focussed on permeability and multiphase flow as this has many uses in the oil and gas industry, even though there are many other uses for pore network modelling, such as solute and reactive transport. For these purposes often stochastically generated networks are used, even though extracted networks might have more possibilities. Future research could focus on making extraction models focussed on reactive transport, and validate these with experiments in order to create a multi-purpose model that could extract a single network from a sample that would work for single and multiphase, solute transport, reactive transport, which could result in the use of pore network models in more research areas than it is used for now.

## 4.2 Fractures

### 4.2.1   Flow behaviour

Visual analysis of the fracture solute transport simulations, show that the solute travels mostly through the fracture, as the permeability in the fracture is higher than in the rest of the sample. This causes a large concentration gradient between the fracture and the matrix, which causes the solute to disperse into the area's surrounding the fracture. This causes a V-shape in the sample up until the moment the solute injection stops. The water without solute also travels the fastest through the sample, causing a V-shape of solute-free water to emerge.  Near the end of the simulation the areas the furthest from the fractures contain the highest concentrations, as the impact of the fracture on these parts is limited. This V-shape is increasingly obvious with larger apertures, because the solute will have a larger difference in permeability compared to the rest of the sample. Clogging of the fracture also reduces the formation of the V-shape, as the fracture does not act as a single pathway anymore, which causes concentration gradients within the fracture itself, in addition to the decreased permeability with clogging.

Clogging of the fractures and smaller apertures seem similar in flow behaviour when observing from the side. For modelling purposes the aperture of an heterogeneous or partially clogged fracture is often approximated as a fracture with a smaller aperture, but the top view of the simulations would suggest that it is not correct to approximate it in that manner in three- dimensional systems for solute transport, as the clogging of the fracture causes increased heterogeneity in concentration in the lateral direction. This causes higher concentration gradients within the fracture, resulting in different flow behaviour. This phenomenon was also found by Hughes and Blunt (1999), who created a heterogeneous network by using different pore throat sizes within the fracture. This suggests the method used in this study, by disconnecting same sized pore throats would be an appropriate method to simulate heterogeneous fractures.

### 3.1.1   Permeability

The permeability for non-clogged fractures is quadratic in relation to the aperture. This makes sense as the permeability of a fracture is a quadratic function of the aperture (eq. 4). However, the fracture does not only increase the permeability by a weighted average of the fracture permeability compared to the permeability of the sample, but due to improved connectivity the permeability increases by more than the expected minimum value. The difference between the expected value and the modelled value is dependent on the aperture size. For small apertures the fracture is not in every case the path of least resistance for the flow, as the pores surrounding the fracture could be favourable. The difference increases until it reaches about 14% increase, which would be the moment the fracture is the path of least resistance for flow coming from most of the surrounding pores. This result is similar to results found by Lv et al. (2019) and  Jiang et al. (2017), who also found a quadratic relation between permeability, but higher permeability values due to increased connectivity.

Increasing the clogging reduces the permeability linearly, until values close to the non-fractured sample are reached, caused by decreased connectivity. For the 10μm sample the 70% clogged permeability is even lower than the non-fractured value, as the increase in permeability caused by the fracture has less impact than the decreased connectivity through the fracture, as these pore throats are disconnected too. For permeability and flow calculations, using the hydraulic aperture compared to the actual aperture does make sense, as the permeability values of different apertures and clogging fractures are similar.

### 3.1.2    Solute transport

The breakthrough curves of the fractured samples become increasingly skewed with increasing aperture, with more solute arriving earlier, with a steep decrease after the peak concentration. Experiments on a field scale showed the same phenomenon (Becker & Shapiro, 2000). This suggests the fracture becomes an increasingly preferential pathway for solutes to travel through. This also explains the fact that peak concentration does not occur at 1.5 pore volume, which is expected, but the majority of the solute arrives sooner. This can be explained by the solute gradients between the fracture and the sample, discussed in 4.1.1. The solute travels through the fracture the fastest, from which the solute disperses into the matrix. The transport through the fracture causes an decrease in arrival time at the boundary, which causes the measured concentration to rise sooner, and causes the skewness of the curve. The majority of the mass is distributed throughout the sample, which makes the peak concentration arrive at the same time as the non-fractured sample. The moment the injection stops, the solute free water also travels the fastest through the fracture, and carries the remaining solute in the fracture out fast. This causes the slope from the peak concentration to the tail to be very steep. The tailing is caused by solute at larger distances from the fracture, where it is less impacted by the fast flow through the fracture, causing this solute to arrive at the same time as it would be with a non-fractured sample, but as the rest of the solute has arrived sooner it creates a long tail.

For clogging fractions the same shape occurs as with aperture variability. No clogging gives the most skewed shape, while high clogging fractures result in shapes similar to the non-fractured medium. This can be explained by the level of preference for the flow to travel through the fracture, which decreases with increased homogeneity. The breakthrough curves also show similar features with increased heterogeneity compared to smaller apertures in the way the shape changes.

The computed dispersivities show unexpected results, showing larger dispersivities than the non-fractured sample with increasing aperture, and at a certain aperture the values fall below the non-fractured value. For non-clogged fractures, as the aperture is large enough to act as a preferential flow path, the solute travelling through the fracture causes a larger spread throughout the sample, increasing the dispersivity values. However, the homogeneous unclogged fracture intrinsically has a low dispersivity, as there are no different flow paths to cause this. If the fracture aperture is too large, a significant part of the solute will travel through the fracture, and the dispersivity will decrease below the original value, as the intrinsic dispersivity of the fracture becomes increasingly important.

Clogging the fracture causes the dispersivity to vary less compared to the original value, as the fracture becomes a less preferential flow path, so the longitudinal dispersion is limited. Also the clogged fracture has an intrinsic dispersivity that with increased clogging becomes increasingly closer to the value of the medium. Even if the fracture functions as a preferential flow path, the dispersivity will change less due to the dispersivity within the fracture, which shows why between apertures of  60μm and 90 μm different clogging fractions will result in the maximum dispersivity. In these location the clogged fracture is the cause of enough dispersivity within the fracture itself, so it does not decrease

yet, and it is considered preferential flow path enough to raise the dispersivity by spreading out the solute longitudinally.

Comparing clogging levels with fracture apertures, the similarity is limited for dispersivity values, as opposed to permeabilities and breakthrough curves. Large apertures will decrease the dispersivity, while the medium range apertures will increase the dispersivity, independent on clogging level. Increasing clogging rates causes the dispersivities to grow closer to the original value. Approximating the hydraulic aperture from actual aperture values will not yield the same result. A fracture with 50 μm aperture, 40% clogging has a similar permeability compared to 40 μm, no clogging, but the dispersivity value are 0.19 mm and 0.27 mm respectively.

In conclusion, in solute transport simulation the heterogeneity of the fracture, in combination with the aperture of the fracture, both matter equally in obtaining good results. Permeabilities can be approximated by using a single homogeneous aperture, and a regular grid as input. The problem is that the actual average aperture might not yield the same results, but if the correct hydraulic aperture is found, it will suffice. If solute transport is the purpose of a model, using an homogeneous fracture will not yield the wanted results, as the shape of the breakthrough curve and the dispersivity are highly sensitive to heterogeneity and clogging within the fracture. The model used in this study consists of equally sized pores within the fracture, and heterogeneity is obtained through disconnection. This simulates clogging decently, but for fractures with higher aperture variation within the fracture the intrinsic dispersivity of the fracture is higher, which will probably result in a smaller decrease in dispersivity for large apertures. It is expected the decrease will still occur, since the 40% and 50% clogging rates still go below the original value.  The increase in dispersivity for medium sized fractures caused by preferential flow through the fracture will also persist.

### 4.2.2   Future research

The model used in this study uses a single fracture. Problems become complicated with fracture networks, which would produce more complicated flow behaviour as the main flow direction might be redirected in the flow direction. Using pore network modelling to create a fracture network is more complicated than using a single fracture as interaction between the fractures is complex and less straightforward as a single fracture, so a method would have to be developed to accurately represent the fracture network in a pore network model. This study has shown that to accurately represent a fracture, a degree of heterogeneity has to be known. From earlier research it is known that the average actual aperture does not represent the hydraulic aperture well, but the hydraulic aperture might also not represent transport properties well, as clogged fractures have different transport properties than fractures with smaller apertures. Further research could be performed on a combination of clogging and variable throat sizes within the pore, to investigate whether the heterogeneity within a fracture can be approximated by disconnecting the pores alone, or whether throat size variability is necessary to obtain the correct results.

# 5. Conclusion

A pore network extraction model is developed, based on the medial axis method(Jiang et al., 2007), the maximal ball method (Dong & Blunt, 2009) and the axis ball method(Yi et al., 2017). The model gives accurate permeability values compared to Lattice Boltzmann simulations for sandstones and carbonates with decent resolution. On the extracted network of the Berea sandstone simulations with different fracture apertures and clogging fractions have been conducted to obtain the effects of fracturing and clogging on permeability and solute transport. The permeability increases quadratically with aperture size. The permeability increases by a larger margin than the estimated permeability increase due to increased connectivity. With increasing aperture, the breakthrough curve becomes increasingly skewed with strong tailing. The dispersivity increases with aperture, until an aperture is reached that carries enough of the solute to reduce the dispersivity value. Clogging of fractures is modelled by reducing the connectivity of pores in the fracture. For permeability it makes no difference if an aperture with a certain clogging level is used, or if a lower aperture is used. For solute transport, the dispersivity remains closer to the value of the matrix, and will increase the dispersivity for larger apertures before it will be reduced below the original value. The balance between the level of preferential flow and the heterogeneity of the fracture determine the dispersivity of a fractured medium. Solute transport in a heterogeneous fracture cannot be approximated by a homogeneous fracture with a smaller aperture.

# 6. References

Al-Kharusi, A. S., & Blunt, M. J. (2007). Network extraction from sandstone and carbonate pore space images. *Journal of Petroleum Science and Engineering*, *56*(4), 219-231.

Adler, P. M., & Thovert, J. F. (1998). Real porous media: Local geometry and macroscopic properties. *Applied Mechanics Reviews*, *51*(9), 537-585.

Adler, P. M., Thovert, J. F., & Mourzenko, V. V. (2013). *Fractured porous media*. Oxford University Press.

Arganda-Carreras, I., Fernandez-Gonzalez, R., Munoz-Barrutia, A. & Ortiz-De-Solorzano, C.(2010). 3D reconstruction of histological sections: Application to mammary gland tissue, *Microscopy Research and Technique*, 73(11), 1019–1029.

Bakke, S., & Øren, P. E. (1997). 3-D pore-scale modelling of sandstones and flow simulations in the pore networks. *Spe Journal*, *2*(02), 136-149.

Baldwin, C. A., Sederman, A. J., Mantle, M. D., Alexander, P., & Gladden, L. F. (1996). Determination and characterization of the structure of a pore space from 3D volume images. *Journal of colloid and interface science*, *181*(1), 79-92.

Becker, M. W., & Shapiro, A. M. (2000). Tracer transport in fractured crystalline rock: Evidence of nondiffusive breakthrough tailing. *Water Resources Research*, *36*(7), 1677-1686.

Berkowitz, B. (2002). Characterizing flow and transport in fractured geological media: A review. *Advances in water resources*, *25*(8-12), 861-884.

Berre, I., Doster, F., & Keilegavlen, E. (2018). Flow in fractured porous media: A review of conceptual models and discretization approaches. *Transport in Porous Media*, 1-22.

Bhattad, P., Willson, C. S., & Thompson, K. E. (2011). Effect of network structure on characterization and flow modeling using X-ray micro-tomography images of granular and fibrous porous media. *Transport in porous media*, *90*(2), 363.

Blunt, M. J. (2001). Flow in porous media—pore-network models and multiphase flow. *Current opinion in colloid & interface science*, *6*(3), 197-207.

Bondino, I., Hamon, G., Kallel, W., & Kac, D. (2013). Relative Permeabilities From Simulation in 3D Rock Models and Equivalent Pore Networks: Critical Review and Way Forward1. *Petrophysics*, *54*(06), 538-546.

Bryant, S., & Blunt, M. (1992). Prediction of relative permeability in simple porous media. *Physical Review A*, *46*(4), 2004.

Bryant, S. L., Mellor, D. W., & Cade, C. A. (1993). Physically representative network models of transport in porous media. *AIChE Journal*, *39*(3), 387-396.

Bryant, S. L., King, P. R., & Mellor, D. W. (1993). Network model evaluation of permeability and spatial correlation in a real random sphere packing. *Transport in Porous Media*, *11*(1), 53-70.

Bultreys, T., Van Hoorebeke, L., & Cnudde, V. (2015). Multi-scale, micro-computed tomography-based pore network models to simulate drainage in heterogeneous rocks. *Advances in Water Resources*, *78*, 36-49.

Bultreys, T., Lin, Q., Gao, Y., Raeini, A.Q., Al Ratrout, A., Bijeljic, B. & Blunt., M.J. (2018). Validation of model predictions of pore-scale fluid distributions during two-phase flow. *Phys. Rev. E* 97(5), 053104

Cardwell, W.T., Parsons, R.L. (1944) Average permeabilities of heterogeneous oil sands, Trans. Am. Inst. Mining Metal. Eng. 160, 34-42.

Coelho, D., Thovert, J. F., & Adler, P. M. (1997). Geometrical and transport properties of random packings of spheres and aspherical particles. *Physical Review E*, *55*(2), 1959.

Dong, H., & Blunt, M. J. (2009). Pore-network extraction from micro-computerized-tomography images. *Physical review E*, *80*(3), 036307.

Durham, W. B., & Bonner, B. P. (1994). Self-propping and fluid flow in slightly offset joints at high effective pressures. *Journal of Geophysical Research: Solid Earth*, *99*(B5), 9391-9399.

van Genuchten, M. Th., Šimůnek, J., Leij, F.L., Toride, N. & Šejna, M. (2012). STANMOD: Model use, calibration and validation, *special issue Standard/Engineering Procedures for Model Calibration and Validation, Transactions of the ASABE*, 5(4), 1353-1366.

Gerritsen, M. G., & Durlofsky, L. J. (2005). Modeling fluid flow in oil reservoirs. *Annu. Rev. Fluid Mech.*, *37*, 211-238.

Hadwiger, H. (1957). Über eibereiche mit gemeinsamer treffgeraden. *Portugaliae mathematica*, *16*(1), 23-29.

Hao, L. & Cheng, P.(2010). Pore-scale simulations on relative permeabilities of porous media by lattice Boltzmann method. *International Journal of Heat and Mass Transfer.,* 53 (9) (2010), 1908-1913.

Helland, J. O., Ryazanov, A. V., & Van Dijke, M. I. J. (2008). Characterization of pore shapes for pore network models. In *ECMOR XI-11th European Conference on the Mathematics of Oil Recovery*.

Hughes, R. G., Blunt, M. J., (1999). Pore-scale modeling of multiphase flow in fractures and matrix/fracture transfer. *Proceedings - SPE Annual Technical Conference and Exhibition*, 1, pp.

Hou, J., Wei, B., Zhou, K., Du, Q., (2018). Representing pore shapes by appropriate polygons in pore network models. (2018) *Journal of Porous Media*, 21 (4), pp. 329-341.

Ioannidis, M. A., & Chatzis, I. (2000). On the geometry and topology of 3D stochastic porous media. *Journal of colloid and interface science*, *229*(2), 323-334.

Jiang, Z., Van Dijke, M. I. J., Sorbie, K. S., & Couples, G. D. (2013). Representation of multiscale heterogeneity via multiscale pore networks. *Water resources research*, *49*(9), 5437-5449.

Jiang, Z., van Dijke, M.I.J., Geiger, S., Ma, J., Couples, G.D., Li, X. (2017) Pore network extraction for fractured porous media. *Advances in Water Resources*, 107, pp. 280-289.

Jiang, Z., Wu, K., Couples, G., Van Dijke, M. I. J., Sorbie, K. S., & Ma, J. (2007). Efficient extraction of networks from three-dimensional porous media. *Water Resources Research*, *43*(12).

Joekar-Niasar, V., & Hassanizadeh, S. M. (2011). Effect of fluids properties on non-equilibrium capillarity effects: Dynamic pore-network modeling. *International Journal of Multiphase Flow*, *37*(2), 198-214.

Joekar-Niasar, V., & Hassanizadeh, S. M. (2012). Analysis of fundamentals of two-phase flow in porous media using dynamic pore-network models: A review. *Critical reviews in environmental science and technology*, *42*(18), 1895-1976.

Joekar Niasar, V., Hassanizadeh, S. M., Pyrak-Nolte, L. J., & Berentsen, C. (2009). Simulating drainage and imbibition experiments in a high-porosity micromodel using an unstructured pore network model. *Water resources research*, *45*(2).

Joekar-Niasar, V., Prodanović, M., Wildenschild, D., & Hassanizadeh, S. M. (2010). Network model investigation of interfacial area, capillary pressure and saturation relationships in granular porous media. *Water Resources Research*, *46*(6).

Köppel, M., Martin, V. & Roberts, J.E. (2019). A stabilized Lagrange multiplier finite-element method for flow in porous media with fractures, *International Journal on Geomathematics* 10(7).

Lee, T.C. , Kashyap R.L. &  Chu, C.N. (1994). Building Skeleton Models via 3-D Medial Surface Axis Thinning Algorithms.  *CVGIP: Graphical Models and Image Processing*, 56(6), 462-478.

Lee, S. H., Lough, M. F., & Jensen, C. L. (2001). Hierarchical modeling of flow in naturally fractured formations with multiple length scales. *Water resources research*, *37*(3), 443-455.

Lenormand, R., Zarcone, C., & Sarr, A. (1983). Mechanisms of the displacement of one fluid by another in a network of capillary ducts. *Journal of Fluid Mechanics*, *135*, 337-353.

Lerdahl, T. R., Oren, P. E., & Bakke, S. (2000, January). A predictive network model for three-phase flow in porous media. In *SPE/DOE Improved Oil Recovery Symposium*. Society of Petroleum Engineers.

Liang, Z. R., Fernandes, C. P., Magnani, F. S., & Philippi, P. C. (1998). A reconstruction technique for three-dimensional porous media using image analysis and Fourier transforms. *Journal of Petroleum Science and Engineering*, *21*(3-4), 273-283.

Liang, Z., Ioannidis, M. A., & Chatzis, I. (2000). Geometric and topological analysis of three-dimensional porous media: pore space partitioning based on morphological skeletonization. *Journal of colloid and interface science*, *221*(1), 13-24.

Lindquist, W. B., Lee, S. M., Coker, D. A., Jones, K. W., & Spanne, P. (1996). Medial axis analysis of void structure in three-dimensional tomographic images of porous media. *Journal of Geophysical Research: Solid Earth*, *101*(B4), 8297-8310.

Lindquist, W. B., Venkatarangan, A., Dunsmuir, J., & Wong, T. F. (2000). Pore and throat size distributions measured from synchrotron X-ray tomographic images of Fontainebleau sandstones. *Journal of Geophysical Research: Solid Earth*, *105*(B9), 21509-21527.

Long, J.C.S., Remer, J.S., Wilson, C.R., Witherspoon, P.A., (1982). Porous media equivalents for networks of discontinuous fractures. *Water Resour. Res*. 18(3), 645–658

Lv, W., Yan, G., Liu, Y.,Liu, X., Du, D., Wang, R. (2019). Effect of fractal fractures on permeability in three-dimensional digital rocks. *Fractals,* 27(1).

Mason, G., & Morrow, N. R. (1991). Capillary behavior of a perfectly wetting liquid in irregular triangular tubes. *Journal of Colloid and Interface Science*, *141*(1), 262-274.

Noetinger, B., & Jarrige, N. (2012). A quasi steady state method for solving transient Darcy flow in complex 3D fractured networks. *Journal of Computational Physics*, *231*(1), 23-38.

Ollion, J., Cochennec, J., Loll, F, Escudé, C & Boudier, T (2013). TANGO: A Generic Tool for High-throughput 3D Image Analysis for Studying Nuclear Organization. *Bioinformatics*, 29(14):1840-1.

Øren, P. E., & Bakke, S. (2002). Process based reconstruction of sandstones and prediction of transport properties. *Transport in porous media*, *46*(2-3), 311-343.

Øren, P. E., & Bakke, S. (2003). Reconstruction of Berea sandstone and pore-scale modelling of wettability effects. *Journal of Petroleum Science and Engineering*, *39*(3-4), 177-199.

Oren, P. E., Bakke, S., & Arntzen, O. J. (1997, January). Extending predictive capabilities to network models. In *SPE Annual Technical Conference and Exhibition*. Society of Petroleum Engineers.

Patzek, T. W. (2000, January). Verification of a complete pore network simulator of drainage and imbibition. In *SPE/DOE Improved Oil Recovery Symposium*. Society of Petroleum Engineers.

Piri, M., & Blunt, M. J. (2005). Three-dimensional mixed-wet random pore-scale network modeling of two-and three-phase flow in porous media. I. Model description. *Physical Review E*, *71*(2), 026301.

Prodanović, M., Lindquist, W. B., & Seright, R. S. (2006). Porous structure and fluid partitioning in polyethylene cores from 3D X-ray microtomographic imaging. *Journal of Colloid and Interface Science*, *298*(1), 282-297.

Prodanović, M., Mehmani, A., & Sheppard, A. P. (2015). Imaged-based multiscale network modelling of microporosity in carbonates. *Geological Society, London, Special Publications*, *406*(1), 95-113.

Raoof, A., & Hassanizadeh, S. M. (2010). A new method for generating pore-network models of porous media. *Transport in porous media*, *81*(3), 391-407.

Raoof, A., & Hassanizadeh, S. M. (2012). A new formulation for pore-network modeling of two-phase flow. *Water Resources Research*, *48*(1).

Raoof, A. , Nick, H.M., Hassanizadeh, S.M., Spiers, C.J.(2013). PoreFlow: A complex pore-network model for simulation of reactive transport in variably saturated porous media, *Computers & Geosciences*, 61, 160-174.

Rasmuson, A., & Neretnieks, I. (1986). Radionuclide transport in fast channels in crystalline rock. *Water Resources Research*, *22*(8), 1247-1256.

Silin, D., & Patzek, T. (2006). Pore space morphology analysis using maximal inscribed spheres. *Physica A: Statistical mechanics and its applications*, *371*(2), 336-360.

Silliman, S. E. (1989). An interpretation of the difference between aperture estimates derived from hydraulic and tracer tests in a single fracture. *Water resources research*, *25*(10), 2275-2283.

Šimůnek, J., van Genuchten, M. Th., Šejna, M., Toride, N., Leij, F.J. (1999). The STANMOD computer software for evaluating solute transport in porous media using analytical solutions of convection-dispersion equation. Versions 1.0 and 2.0, *IGWMC - TPS - 71, International Ground Water Modeling Center*, Colorado School of Mines, Golden, Colorado, 32pp.

Thovert, J. F., Salles, J., & Adler, P. M. (1993). Computerized characterization of the geometry of real porous media: their discretization, analysis and interpretation. *Journal of microscopy*, *170*(1), 65-79.

Vogel, H. J., & Roth, K. (2001). Quantitative morphology and network representation of soil pore structure. *Advances in water resources*, *24*(3-4), 233-242.

Warren, J. E., & Root, P. J. (1963). The behavior of naturally fractured reservoirs. *Society of Petroleum Engineers Journal*, *3*(03), 245-255.

Xiong, Q., Baychev, T. G., & Jivkov, A. P. (2016). Review of pore network modelling of porous media: experimental characterisations, network constructions and applications to reactive transport. *Journal of contaminant hydrology*, *192*, 101-117.

Yi, Z., Lin, M., Jiang, W., Zhang, Z., Li, H., and Gao, J. ( 2017), Pore network extraction from pore space images of various porous media systems, *Water Resour. Res.*, 53, 3424– 3445,

Zhang, M., Xu, K., He, Y., Jivkov, A.P (2014) Pore-scale modelling of 3D moisture distribution and critical saturation in cementitious materials. *Construction and Building Materials,* 64, pp. 222-230.